A novel 2.5D spectral approach for studying thin-walled waveguides with fluid-acoustic interaction

A. Romero[a,*], F.J. Cruz-Muñoz[a], A. Tadeu[b], P. Galvín[a]

[a] *Escuela Técnica Superior de Ingeniería, Universidad de Sevilla, Camino de los Descubrimientos, 41092 Sevilla, Spain*
[b] *Department of Civil Engineering, University of Coimbra, Pólo II, Rua Luís Reis Santos, 3030-788 Coimbra, Portugal*

Abstract

This paper presents a novel formulation of two spectral elements to study guided waves in coupled problems involving thin-walled structures and fluid-acoustic enclosures. The aim of the proposed work is the development of a new efficient computational method to study problems where geometry and properties are invariant in one direction, commonly found in the analysis of guided waves. This assumption allows using a two-and-a-half dimensional (2.5D) spectral formulation in the wavenumber-frequency domain. The novelty of the proposed work is the formulation of spectral plate and fluid elements with an arbitrary order in 2.5D. A plate element based on a Reissner-Mindlin/Kirchhoff-Love mixed formulation is proposed to represent the thin-walled structure. This element uses C^0 approximation functions to overcome the difficulties to formulate elements with an arbitrary order from C^1 functions. The proposed element uses a substitute transverse shear strain field to avoid shear locking effects. Three benchmark problems are studied to check the convergence and the computational effort for different $h-p$ strategies. Accurate results are found with an appropriate combination of element size and order of the approximation functions allowing at least six nodes per wavelength. The effectiveness of the proposed elements is demonstrated studying the wave propagation in a water duct with a flexible side and an acoustic cavity coupled to a Helmholtz resonator.

Keywords: Fluid waveguide, solid waveguide, two-and-a-half dimension, spectral element method, acoustic, shear locking

---

1. Introduction

Time-harmonic wave propagation is a fundamental subject related to many engineering applications such as fluid acoustics, scattering in solids, electromagnetic fields, etc. The propagation of acoustic waves triggered by static and moving pressure sources, the vibration assessment and the acoustic insulation all involve fluid-solid interaction and it should be considered rigorously. The wave propagation in waveguides has been thoroughly analysed using either analytic or numerical methods.

---

[*] Corresponding author
Email address: `aro@us.es` (A. Romero)

There is a large number of works about the characterization of acoustic and elastic waveguides based on analytical methods. Among others, Pagneux et al. [1] studied the wave propagation in acoustic waveguides with variable cross-section using a multimodal decomposition methodology. This approach considered implicitly the radiation condition for an infinite length medium. Later, Pagneux and Maurel [2] formulated a multimodal approach to represent Lamb wave propagation in elastic waveguides. Lawrie [3] presented a hybrid method for the solution of rectangular ducts with flexible walls. The author defined some analytic expressions for the characteristic equations and natural waveforms corresponding to acoustic modes propagation in the frequency range from 0 to 1500 Hz. Athanassoulis et al. [4] used a consistent coupled-mode method and the finite element method (FEM) in problems related to underwater acoustic waveguides. They compared their results for low-frequency sources with the coupled-mode method. The computed results from the three methods were in good agreement except at frequencies close to resonances of the system. Recently, Maurel et al. [5] proposed an improved version of the multimodal method in acoustic waveguides. The introduction of a boundary mode in the multimodal method improved significantly the efficiency and the accuracy of the methodology.

The numerical analysis of waveguides is advantageous in the representation of arbitrary cross-section geometries and avoiding the complexity of coupling analytically fluid and solid subdomains. Nevertheless, the previous analytical or hybrid methods easily account for the radiation condition in waveguides, which is a much more difficult task in numerical methods such as finite or boundary element (BEM) formulations. Moreover, the computational effort in numerical methods is quite higher than in analytical procedures. The numerical analysis of waveguides becomes much simpler if the medium is invariant in one direction. Such a situation is referred to as a two-and-a-half dimensional (2.5D) problem [6]. The 2.5D formulation is based on the Fourier decomposition of the three-dimensional (3D) problem into two dimensional (2D) problems with different wavenumbers. Gravrić [7] developed a 2.5D thin-shell finite element for studying thin-walled waveguides. Later, Gravrić [8] analysed the wave propagation in a free rail using 2.5D solid finite elements. Mencik and Ichchou [9] presented a finite element formulation for the representation of wave propagation in a fluid-filled guided structure. Nilsson and Finnveden [10] proposed a waveguide finite element to study fluid-filled ducts and pipes. Romero et al. [11, 12] and Tadeu et al. [13] presented a coupled finite-boundary element formulation in 2.5D to study noise and vibration in tunnels.

Although the FEM has been used in several works to represent accurately the fluid and solid scattering waves for the low-frequency range, at higher frequencies this method could not provide reliable results due to so-called pollution effects [14, 15]. The accuracy of the numerical solution deteriorates as the wavenumber increases and the commonly employed rule of a certain number of elements per wavelength [16] is not sufficient. Ihlenburg and Babuška [17, 18] demonstrated that the pollution effect of the FEM to study acoustic problems is related to the stability of the Helmholtz differential operator at high wavenumbers. The $h-$FEM methodology has proven to be useless at high frequencies due to the high computational effort necessary to represent small wavelengths [19]. Many works suggest the use of high-order elements ($p-$FEM) to improve the convergence rate of the $h-$FEM. In this case, higher order element shape functions are used to obtain results with reasonable accuracy. Deraemaeker et al. [20] studied several finite element methodologies for solving the Helmholtz equation. They concluded that the $p-$FEM drastically reduces the pollution error. Belibassakis et al. [21] presented a model based on a modal expansion for studying harmonic wave propagation and scattering problems in inhomogeneous layered waveguides governed by the Helmholtz equation. $h-$ and $p-$FEM were applied for the solution of both the local vertical eigenvalue problem and the resulting coupled mode system, exhibiting robustness and good rates of convergence.

Alternatively, spectral element methodologies (SEM) have been developed [22, 23]. In these methodologies, the field variables are represented by high-order interpolation shape functions usually defined at the Legendre-Gauss-Lobatto (LGL) integration points. Vos et al. [24] presented an efficient implementation of a spectral/$h-p$ element method for problems with smooth and non-smooth solutions. They analysed the specific combination of mesh size and polynomial order to minimise the computational cost. Mehdizadeh and Paraschivoiu [25] compared a SEM and a second-order FEM. These authors concluded that the two-dimensional SEM leads to a fewer number of elements per wavelength and less computational cost in terms of both, memory and computational time, for the same accuracy. Petersen et al. [26] and Biermann et al. [27] studied several shape function families for acoustic simulations. They concluded that the SEM is an efficient method even at the high-frequency range for solving the Helmholtz equation. Recently, Christodoulou et al. [28] presented a spectral element to study the solution of the 2D Helmholtz equation. They solved problems involving evanescent waves and high wavenumbers, concluding that the SEM provided accurate results.

This paper proposes a new 2.5D plate element to represent waveguides. As regards to the formulation of this element with infinite length, there are some analytical and numerical models for plate analysis to be cited. However, it should be indicated that the following works address the behaviour of plates with finite dimensions.

In 60's and 70's several pioneering analytical models [29, 30, 31, 32] were developed. These models were based on the extension of the known Kantorovich's method [33] for the analysis of slab structures. The use of this technique for the analysis of plates under Kirchoff-Love's theory is due to Cheung [34] who denominated the methodology finite strip method. This method was extended to Reissner-Mindlin theory for thick slabs [32]. The treatment of the shear locking has been deeply studied in many researches. Hughes and Franca [35] demonstrated that the convergence of plate formulations based on Reissner-Mindlin theory applied to thin slabs is achieved for any element formulated by interpolation functions with enough order. Then, techniques like reduced or selective integration, discrete Kirchhoff conditions, or special transverse shear strain interpolation are not required. The number of papers published during the last years shows the increasing interest in this topic [36, 37, 38, 39, 40].

Among others, the following high-order formulations have been recently developed to represent plate structure behaviour. Zrahia and Bar-Yoseph [41] proposed a Reissner-Mindlin plate spectral element for a rectangular geometry. The authors concluded that the shear locking phenomenon for slender plates is eliminated by the use of high-order shape functions which is in agreement with Reference [35]. Chakraborty and Gopalakrishnan [42] presented a spectral thin plate element to study wave propagation in an anisotropic material. This element was used to analyse a plate with ply drops and to represent the Lamb waves. Birgersson et al. [43] derived the equation of motion for a rectangular plate strip to represent a spectral superelement plate as built up from a number of such strips. Zak [44] developed a spectral plate element based on Chebyshev polynomials of the first kind to study symmetric and anti-symmetric modes of the Lamb waves. The high-order polynomials used for the approximation of all in-plane displacements avoided the shear locking phenomena. Brito and Sprague [45] proposed a spectral element based on the Reissner-Mindlin formulation with mixed reduced quadrature getting a shear locking free element. Sprague and Purkayastha [46] proposed a Legendre spectral element for composite plates based on the Reissner-Mindlin theory. They also found the Legendre spectral element was shear-locking free using a nodal quadrature.

This paper presents a novel 2.5D approach based on the SEM to study wave propagation problems with invariant cross-section acting as waveguides including the fluid-structure interaction (FSI). The structure is modelled as a thin-walled waveguide using a plate element based on the Kirchhoff-Love and the Reissner-Mindlin formulations. The shear effect of dispersive waves with short wavelengths propagating along the longitudinal direction is neglected due to the infinite length of the plate. The small rotation approach is considered for the analysis of plates rather than a more general element able to represent moderate or large rotations [47]. The plate element variables are all kinematic: displacements and independent rotations. As only C^0 continuity is required, isoparametric elements may be employed, which results in several advantages [35] in relation to the 2.5D thin plate elements proposed by Gavrić [7]. However, the infinite length in one direction makes the element to be sensitive to shear locking even using a high-order formulation. The proposed plate element formulation employs a stabilised auxiliary shear strain field instead of reduced or selective integration procedures to avoid this effect[48, 49, 50]. The fluid spectral element is derived from the 2.5D FEM based on the Helmholtz equation [11].

The outline of this paper is as follows. First, the numerical model consisting of the spectral element formulations to represent FSI waveguides is developed. The stabilised spectral element for thin-walled guides, the spectral fluid-acoustic element and the coupling procedure are presented in detail. Later, the proposed methodology is verified from three benchmark problems. Finally, the coupled formulation is used to study the wave propagation in an acoustic waveguide with a flexible wall [51, 52] and an acoustic cavity coupled to a Helmholtz resonator [53]. The basis of the proposed method and a brief analysis of a thin-walled waveguided interaction with a fluid duct were presented at EURODYN2017 conference [54].

2. Numerical model

The numerical model is based on a 2.5D spectral element formulation for structure (Ω_s) and fluid (Ω_f) subdomains (Figure 1). The structural behaviour is governed by the equilibrium equation for a continuum solid and the fluid by the Helmholtz acoustic wave equation, accounting for Neumann and Dirichlet boundary conditions (BC). The coupling between both formulations is done by imposing appropriate boundary conditions at the fluid-structure interface Γ_q. Equilibrium of normal pressure, compatibility of normal displacement and null shear stresses are imposed at the interface Γ_q. The governing equations and the boundary conditions can be written as follows:

$$\begin{cases} \nabla \cdot \boldsymbol{\sigma} + \mathbf{b} = \omega^2 \rho_s \mathbf{u}_s & \text{in}\,\Omega_s\,, \quad \text{with BC} \\ \nabla^2 p + k_f^2 p = 0 & \text{in}\,\Omega_f\,, \quad \text{with BC} \\ \mathbf{u}_s^T \mathbf{n}_{qs} = \mathbf{u}_f^T \mathbf{n}_{qf} & \text{in}\,\Gamma_q \\ \left(\boldsymbol{\sigma} \mathbf{n}_{qs}\right)^T \mathbf{n}_{qs} + p = 0 & \text{in}\,\Gamma_q \end{cases} \tag{1}$$

where the variables in the solid equation are the stress tensor $\boldsymbol{\sigma}$, the body force vector $\mathbf{b}$, the displacement vector $\mathbf{u}_s$, the solid density ρ_s and the angular frequency ω. The Helmholtz equation defines the pressure field p for a fluid wavenumber $k_f = \omega / c_f$, where c_f is the sound wave propagation velocity. Moreover, the coupling conditions include the fluid particle displacements $\mathbf{u}_f$ and the outward solid and fluid normals at the interface Γ_q, $\mathbf{n}_{qs}$ and $\mathbf{n}_{qf}$ (with $\mathbf{n}_{qs} = -\mathbf{n}_{qf}$), respectively.

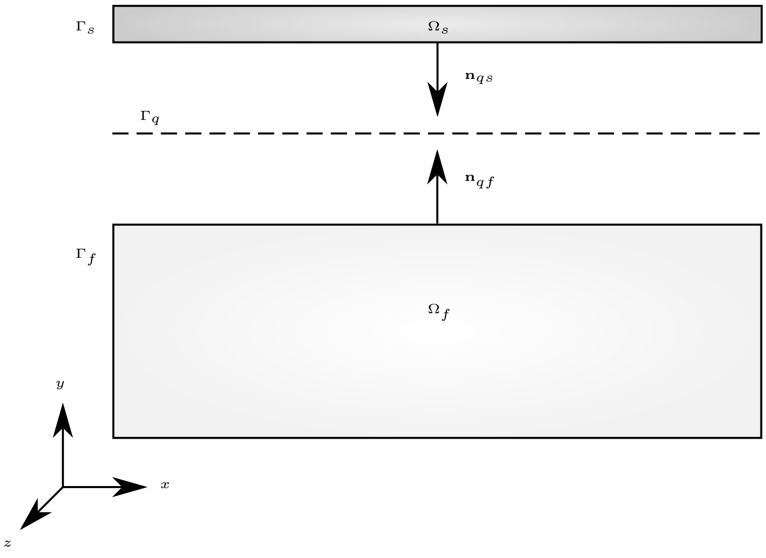

Figure 1: Fluid-structure subdomains.

The 2.5D formulation is addressed defining a characteristic field for the elastic and the acoustic waveguides at point $\mathbf{x} = \mathbf{x}(x, y, z)$ as [7, 8]:

$$\widehat{f}(\mathbf{x}, k_z, \omega) = \widetilde{f}(\widetilde{\mathbf{x}}, k_z, \omega)e^{-ik_z z} \tag{2}$$

where $\widehat{f}(\mathbf{x}, k_z, \omega)$ is the frequency-wavenumber representation of an unknown variable (e.g. displacement, force or pressure), $\widetilde{\mathbf{x}} = \mathbf{x}(x, y)$ and $i = \sqrt{-1}$. The 3D solution is computed as the superposition of 2D solutions with different wavenumber k_z:

$$f(\mathbf{x}, \omega) = \int_{-\infty}^{+\infty} \widetilde{f}(\widetilde{\mathbf{x}}, k_z, \omega)e^{-ik_z z}\, dk_z \tag{3}$$

Table 1 summarises the notation used in the following sections. The spatial representation and the frequency-wavenumber dependence is implicitly considered for simplicity in the notation.

Table 1: List of symbols

$\mathbf{x} = \mathbf{x}(x, y, z)$	Spatial representation in 3D
$\widetilde{\mathbf{x}} = \mathbf{x}(x, y)$	Spatial representation in 2.5D
$f = f(\mathbf{x}, \omega)$	Frequency representation
$\widehat{f} = \widehat{f}(\mathbf{x}, k_z, \omega) = \widetilde{f}(\widetilde{\mathbf{x}}, k_z, \omega)e^{-ik_z z}$	Frequency-wavenumber representation
$\square_s$	Structure variable
$\square_f$	Fluid variable
$\square_\chi$	Bending variable
$\square_\gamma$	Shear variable
$\square^e$	Elemental variable
$\square^i$	Nodal variable

2.1. The 2.5D stabilised plate spectral element

This section presents a stabilised spectral element based on a Reissner-Mindlin/ Kirchhoff-Love mixed formulation. The plate is defined by the subdomain Ω_s, the boundary Γ_s and the thickness t (Figure 2). The plate dimensions are $W \times L$. Both, the cross section and the material properties remain invariant along the z axis.

The displacement field is denoted by the transverse displacement u_y and the rotations θ_x and θ_z at the plate mid-surface:

$$\mathbf{u}_s = [u_y, \theta_x, \theta_z]^T \tag{4}$$

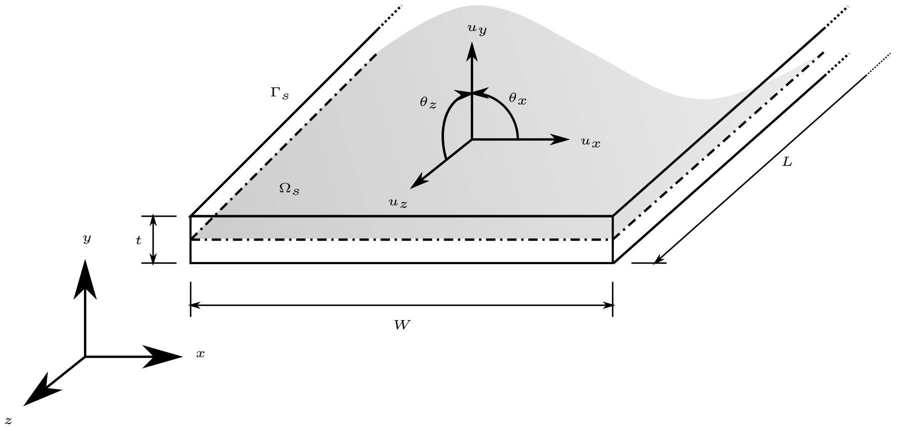

Figure 2: Plate representation.

Plate displacements of any point are approximated as [55]:

$$u_x = -y\theta_x = -y\left(\frac{\partial u_y}{\partial x} + \phi_x\right) \tag{5}$$

$$u_y = u_y \tag{6}$$

$$u_z = -y\theta_z = -y\left(\frac{\partial u_y}{\partial z} + \phi_z\right) \tag{7}$$

where ϕ_x and ϕ_z are the rotations of the mid-surface normal due to the shear deformation.

The 2.5D formulation assumes uniformity of the geometry along the z axis. Therefore, the plate dimension L leads to an infinite length [7]. This consideration implies that the slenderness ratio L/t goes to infinity. Then, the structure behaves as a thin plate neglecting the contribution of shear deformation ϕ_z to the longitudinal displacement u_z.

With this thin-plate assumption, Equations (5-7) can be written in the frequency-wavenumber domain as follows:

$$\widehat{u}_x = -y\widehat{\theta}_x \tag{8}$$

$$\widehat{u}_y = \widehat{u}_y \tag{9}$$

$$\widehat{u}_z = yik_z\widehat{u}_y \tag{10}$$

It can be seen from Equations (8-10) that the plate displacements are defined by two degrees of freedom, with $\widehat{\mathbf{u}}_s = \left[\widehat{u}_y, \widehat{\theta}_x\right]^T$, according to a Reissner-Mindlin/Kirchhoff-Love mixed formulation.

Voigt notation is used to express the small strain tensor as:

$$\begin{aligned}\widehat{\boldsymbol{\varepsilon}} &= \left[\widehat{\varepsilon}_x, \widehat{\varepsilon}_y, \widehat{\varepsilon}_z, \widehat{\gamma}_{xy}, \widehat{\gamma}_{xz}, \widehat{\gamma}_{yz}\right]^T \\ &= \left[\frac{\partial \widehat{u}_x}{\partial x}, \frac{\partial \widehat{u}_y}{\partial y}, \frac{\partial \widehat{u}_z}{\partial z}, \frac{\partial \widehat{u}_x}{\partial y} + \frac{\partial \widehat{u}_y}{\partial x}, \frac{\partial \widehat{u}_x}{\partial z} + \frac{\partial \widehat{u}_z}{\partial x}, \frac{\partial \widehat{u}_y}{\partial z} + \frac{\partial \widehat{u}_z}{\partial y}\right]^T\end{aligned} \tag{11}$$

The strain $\widehat{\varepsilon}_y$ is null since it is considered that the vertical displacement $\widehat{u}_y$ is constant throughout the plate thickness. Also, the shear strain $\widehat{\gamma}_{yz}$ is null due to the thin plate behaviour considered along the z direction. Then, according to Equations (8-11) and omitting $\widehat{\varepsilon}_y$ and $\widehat{\gamma}_{yz}$, the strain tensor becomes:

$$\widehat{\boldsymbol{\varepsilon}} = \left(\begin{array}{c} \widehat{\varepsilon}_x \\ \widehat{\varepsilon}_z \\ \widehat{\gamma}_{xz} \\ \hline \widehat{\gamma}_{xy} \end{array} \right) = \left(\begin{array}{c} -y\partial\widehat{\theta}_x/\partial x \\ yk_z^2\widehat{u}_y \\ -\widehat{\theta}_x + \partial\widehat{u}_y/\partial x \\ \hline y\left(ik_z\widehat{\theta}_x + ik_z\partial\widehat{u}_y/\partial x\right) \end{array} \right) = \left(\begin{array}{c} \widehat{\boldsymbol{\chi}} \\ \hline \widehat{\boldsymbol{\gamma}} \end{array} \right) \tag{12}$$

which can be separated in bending $\widehat{\boldsymbol{\chi}}$ and transverse shear $\widehat{\boldsymbol{\gamma}}$ contributions.

A linear isotropic material law defines the stress-strain relation:

$$\widehat{\boldsymbol{\sigma}} = \mathbf{C}\widehat{\boldsymbol{\varepsilon}} \tag{13}$$

where the constitutive matrix $\mathbf{C}$ is given by:

$$\mathbf{C} = \begin{bmatrix} \mathbf{C}_\chi & \mathbf{0} \\ \mathbf{0} & C_\gamma \end{bmatrix} \qquad \text{with} \qquad \mathbf{C}_\chi = \frac{Et^3}{12(1-\nu^2)} \begin{bmatrix} 1 & \nu & 0 \\ \nu & 1 & 0 \\ 0 & 0 & \dfrac{1-\nu}{2} \end{bmatrix}, \qquad C_\gamma = \kappa G t \tag{14}$$

E being the Young's modulus, G the shear modulus, ν the Poisson's ratio, $\kappa = 5/6$ the shear correction factor for a slab with constant thickness, and $\mathbf{C}_\chi$ and C_γ are the constitutive matrices for bending and shear components.

The proposed spectral element formulation is addressed from the virtual work principle for 2D problems with different wavenumber k_z, which states [7]:

$$-\omega^2 \int_{\Omega_s} \delta\widehat{\mathbf{u}}_s \rho_s \widehat{\mathbf{u}}_s \, d\Omega + \int_{\Omega_s} \delta\widehat{\boldsymbol{\varepsilon}}\widehat{\boldsymbol{\sigma}} \, d\Omega = \int_{\Omega_s} \delta\widehat{\mathbf{u}}_s \rho_s \widehat{\mathbf{b}} \, d\Omega + \int_{\Gamma_s} \delta\widehat{\mathbf{u}}_s \widehat{\mathbf{t}} \, d\Gamma \tag{15}$$

where $\rho_s\widehat{\mathbf{b}}$ is the body force and $\widehat{\mathbf{t}}$ is the traction at the boundary Γ_s. A variable preceded by δ denotes a compatible variation of the displacement or strain field.

Equation (15) implicitly considers the dependence along the longitudinal coordinate z on $e^{-ik_z z}$. Assuming an invariant longitudinal geometry, Equation (15) must be fulfilled if:

$$-\omega^2 \int_{A_s} \delta\widetilde{\mathbf{u}}_s \rho_s \widetilde{\mathbf{u}}_s \, dA + \int_{A_s} \delta\widetilde{\boldsymbol{\varepsilon}}\widetilde{\boldsymbol{\sigma}} \, dA = \int_{A_s} \delta\widetilde{\mathbf{u}}_s \rho_s \widetilde{\mathbf{b}} \, dA + \int_{\Sigma_s} \delta\widetilde{\mathbf{u}}_s \widetilde{\mathbf{t}} \, d\Sigma \tag{16}$$

where A_s and Σ_s are the cross section of Ω_s and its boundary line, respectively.

The mid-surface of the plate is discretised into n_{el} elements with shape functions of order p ($p+1$ nodes), each one with cross section A_s^e and boundary Σ_s^e. The approximated displacement field for an element is defined by its nodal values $\widetilde{\mathbf{u}}_s^{e,i}$ and the shape functions ϕ^i as:

$$\sum_{i=1}^{p+1} \phi^i \widetilde{\mathbf{u}}_s^{e,i} = \boldsymbol{\phi}\widetilde{\mathbf{u}}_s^e \tag{17}$$

Then, the element strain tensor can be defined by Equation (12) as:

$$\widetilde{\boldsymbol{\chi}}^e = \sum_{i=1}^{p+1} \begin{pmatrix} -y\widetilde{\theta}_x^{e,i}\partial\phi^i/\partial x \\ yk_z^2\phi^i\widetilde{u}_y^{e,i} \\ y\left(ik_z\phi^i\widetilde{\theta}_x^{e,i} + ik_z\widetilde{u}_y^{e,i}\partial\phi^i/\partial x\right) \end{pmatrix} = \sum_{i=1}^{p+1}\left[\mathbf{B}_{\chi 0}^i + ik_z\mathbf{B}_{\chi 1}^i + k_z^2\mathbf{B}_{\chi 2}^i\right]\widetilde{\mathbf{u}}_s^{e,i} = \sum_{i=1}^{p+1}\left[\widetilde{\mathbf{B}}_\chi^i\right]\widetilde{\mathbf{u}}_s^{e,i} = \widetilde{\mathbf{B}}_\chi^e\widetilde{\mathbf{u}}_s^e \tag{18}$$

$$\widetilde{\boldsymbol{\gamma}}^e = \sum_{i=1}^{p+1}\left(-\phi^i\widetilde{\theta}_x^{e,i} + \widetilde{u}_y^{e,i}\partial\phi^i/\partial x \right) = \sum_{i=1}^{p+1}\left[\mathbf{B}_{\gamma 0}^i\right]\widetilde{\mathbf{u}}_s^{e,i} = \mathbf{B}_{\gamma 0}^e\widetilde{\mathbf{u}}_s^e \tag{19}$$

The frequency-wavenumber matrix relating bending strain and displacement is defined as $\widetilde{\mathbf{B}}_\chi^e$. From Equation (19) it is deduced that the transverse shear contribution does not depend on the longitudinal wavenumber, k_z, according with the assumption of thin plate behaviour in that direction. The total element strain is given by $\widetilde{\boldsymbol{\varepsilon}}^e = \widetilde{\boldsymbol{\chi}}^e + \widetilde{\boldsymbol{\gamma}}^e = \sum_{i=1}^{p+1}\widetilde{\mathbf{B}}^i\widetilde{\mathbf{u}}_s^{e,i} = \widetilde{\mathbf{B}}^e\widetilde{\mathbf{u}}_s^e$, with $\widetilde{\mathbf{B}}^i = \widetilde{\mathbf{B}}_\chi^i + \mathbf{B}_{\gamma 0}^i$.

Then, substituting Equations (17-19) into Equation (16), the virtual work principle expression for an element yields:

$$-\omega^2\int_{A_s^e}\delta\widetilde{\mathbf{u}}_s^{e^T}\boldsymbol{\phi}^T\rho_s\phi\widetilde{\mathbf{u}}_s^e\,dA + \int_{A_s^e}\delta\widetilde{\mathbf{u}}_s^{e^T}\widetilde{\mathbf{B}}^{e^T}\mathbf{C}\widetilde{\mathbf{B}}^e\widetilde{\mathbf{u}}_s^e\,dA = \int_{A_s^e}\delta\widetilde{\mathbf{u}}_s^{e^T}\boldsymbol{\phi}^T\rho_s\widetilde{\mathbf{b}}^e\,dA + \int_{\Sigma_s^e}\delta\widetilde{\mathbf{u}}_s^{e^T}\boldsymbol{\phi}^T\widetilde{\mathbf{t}}^e\,d\Sigma \tag{20}$$

The integral involving the internal work in Equation (20) becomes:

$$\begin{aligned}
&\int_{A_s^e}\delta\widetilde{\mathbf{u}}_s^{e^T}\widetilde{\mathbf{B}}^{e^T}\mathbf{C}\widetilde{\mathbf{B}}^e\widetilde{\mathbf{u}}_s^e\,dA \\
&= \int_{A_s^e}\delta\widetilde{\mathbf{u}}_s^{e^T}\left[\mathbf{B}_{\chi 0}^{e^T}\mathbf{C}_\chi\mathbf{B}_{\chi 0}^e\right]\widetilde{\mathbf{u}}_s^e\,dA \\
&+ \int_{A_s^e}\delta\widetilde{\mathbf{u}}_s^{e^T}\left[\mathbf{B}_{\gamma 0}^{e^T}C_\gamma\mathbf{B}_{\gamma 0}^e\right]\widetilde{\mathbf{u}}_s^e\,dA \\
&+ ik_z\int_{A_s^e}\delta\widetilde{\mathbf{u}}_s^{e^T}\left[\mathbf{B}_{\chi 0}^{e^T}\mathbf{C}_\chi\mathbf{B}_{\chi 1}^e + \mathbf{B}_{\chi 1}^{e^T}\mathbf{C}_\chi\mathbf{B}_{\chi 0}^e\right]\widetilde{\mathbf{u}}_s^e\,dA \\
&+ k_z^2\int_{A_s^e}\delta\widetilde{\mathbf{u}}_s^{e^T}\left[\mathbf{B}_{\chi 0}^{e^T}\mathbf{C}_\chi\mathbf{B}_{\chi 2}^e - \mathbf{B}_{\chi 1}^{e^T}\mathbf{C}_\chi\mathbf{B}_{\chi 1}^e + \mathbf{B}_{\chi 2}^{e^T}\mathbf{C}_\chi\mathbf{B}_{\chi 0}^e\right]\widetilde{\mathbf{u}}_s^e\,dA \\
&+ ik_z^3\int_{A_s^e}\delta\widetilde{\mathbf{u}}_s^{e^T}\left[\mathbf{B}_{\chi 1}^{e^T}\mathbf{C}_\chi\mathbf{B}_{\chi 2}^e + \mathbf{B}_{\chi 2}^{e^T}\mathbf{C}_\chi\mathbf{B}_{\chi 1}^e\right]\widetilde{\mathbf{u}}_s^e\,dA \\
&+ k_z^4\int_{A_s^e}\delta\widetilde{\mathbf{u}}_s^{e^T}\left[\mathbf{B}_{\chi 2}^{e^T}\mathbf{C}_\chi\mathbf{B}_{\chi 2}^e\right]\widetilde{\mathbf{u}}_s^e\,dA
\end{aligned} \tag{21}$$

Then, Equation (20) is written as follows eliminating the displacement vector $\delta\widetilde{\mathbf{u}}_s^e$:

$$\left[-\omega^2\mathbf{M}^e + \mathbf{K}_{\chi 0}^e + \mathbf{K}_{\gamma 0}^e + ik_z\mathbf{K}_{\chi 1}^e + k_z^2\mathbf{K}_{\chi 2}^e + ik_z^3\mathbf{K}_{\chi 3}^e + k_z^4\mathbf{K}_{\chi 4}^e\right]\widetilde{\mathbf{u}}^e = \widetilde{\mathbf{f}}^e \tag{22}$$

where $\mathbf{M}^e$ is the element mass matrix, $\mathbf{K}_{\chi 0}^e$, $\mathbf{K}_{\gamma 0}^e$, $\mathbf{K}_{\chi 1}^e$, $\mathbf{K}_{\chi 2}^e$, $\mathbf{K}_{\chi 3}^e$, and $\mathbf{K}_{\chi 4}^e$ are the stiffness element matrices and $\widetilde{\mathbf{f}}^e$ is a vector that collects the forces applied in the element. These matrices are defined according to Equation 21.

Once the subdomain A_s is discretised into n_{el} elements, Equation (16) can be written as:

$$\widetilde{\mathbf{K}}\widetilde{\mathbf{u}}_s = \widetilde{\mathbf{f}} \tag{23}$$

where $\widetilde{\mathbf{K}} = -\omega^2\mathbf{M} + \mathbf{K}_{\chi 0} + \mathbf{K}_{\gamma 0} + ik_z\mathbf{K}_{\chi 1} + k_z^2\mathbf{K}_{\chi 2} + ik_z^3\mathbf{K}_{\chi 3} + k_z^4\mathbf{K}_{\chi 4}$ is the equivalent dynamic stiffness matrix, being $\mathbf{K}_{\chi 0}$, $\mathbf{K}_{\gamma 0}$, $\mathbf{K}_{\chi 1}$, $\mathbf{K}_{\chi 2}$, $\mathbf{K}_{\chi 3}$, and $\mathbf{K}_{\chi 4}$ the assembled global stiffness matrices, and $\mathbf{M}$ is the assembled global mass matrix.

This work uses LGL polynomials of order p as shape functions for both geometry and displacement approximations. Nodes in the natural coordinate $\xi \in [-1, 1]$ are at the LGL points, which are the zeros of the following expression:

$$(1-\xi^2)\frac{\partial \phi}{\partial \xi} = 0 \tag{24}$$

The shape interpolation functions for a plate element of order p are computed from the Lagrange polynomials on the LGL integration points given by Equation (24):

$$\phi^i = \prod_{\substack{j=1 \\ j\neq i}}^{p+1} \frac{\xi - \xi_i}{\xi_j - \xi_i} \tag{25}$$

Shape function ϕ^i and its derivatives are symbolically computed for any arbitrary element order. Figure 3 shows the shape interpolation functions for a spectral element with order $p = 6$.

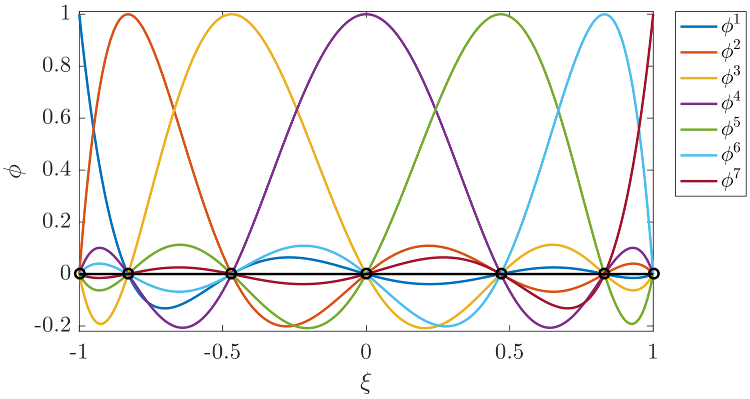

Figure 3: Element shape functions ϕ^i for a plate spectral element with order $p = 6$. Nodal coordinates are marked by circles.

The formulation presented in this work exhibits shear locking for high slenderness ratios W/t when the element stiffness shear matrix $\mathbf{K}^e_{\gamma 0}$ is computed according to Equation (21). Next, a shear locking free 2.5D plate spectral element is developed using a stabilisation of the stiffness shear matrix.

The stabilisation is based on fulfilling the condition that transverse shear strain must be zero for the limiting thin-plate behavior [48, 49, 50]. Then, the proposed element uses a shear strain field $\widetilde{\gamma}^{e'}_{xy}$ to compute the shear deformation term in Equation (19). The transverse shear strain element field $\widetilde{\gamma}^{e}_{xy}$ is approximated by independent interpolation shape functions $\boldsymbol{\phi}'$ and the shear strain $\widetilde{\gamma}_{xy}^{e,i'}$ at p internal points within the element:

$$\widetilde{\gamma}_{xy}^{e} = \sum_{i=1}^{p} \phi^{i'} \widetilde{\gamma}_{xy}^{e,i'} \tag{26}$$

For the sake of clarity, Figure 4 shows the interpolation shape functions $\boldsymbol{\phi}$ and $\boldsymbol{\phi}'$ for an element with order $p = 2$ in natural coordinates. The auxiliary internal points ξ' are found at the Gauss-Legendre points, while the element nodes remain at the Legendre-Gauss-Lobatto (LGL) points. The interpolation shape functions $\boldsymbol{\phi}'$ are one order lower than the functions $\boldsymbol{\phi}$. The use of $\boldsymbol{\phi}'$ as interpolation shape functions leads to the fulfilment of zero transverse shear strain at ξ' for thin-plate, which yields to a shear-locking free formulation.

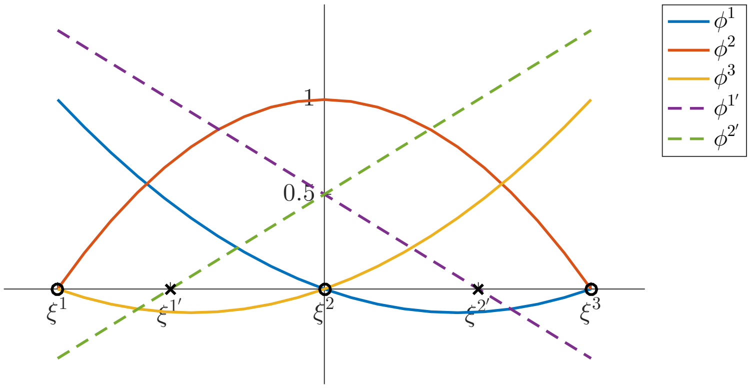

Figure 4: Shape functions for a spectral element $p = 2$. Element nodes (circles) and internal points for shear strain $\widetilde{\gamma}_{xy}$ (crosses).

Equation (26) is rewritten using the auxiliary field $\widetilde{\gamma}'_{xy}$ expressed in the natural coordinate, $\widetilde{\gamma}'_{\xi}$:

$$\widetilde{\gamma}_{xy}^{e} = \mathbf{J}^{-1} \sum_{i=1}^{p} \phi^{i'} \widetilde{\gamma}_{\xi}^{e,i'} = \mathbf{J}^{-1} \widetilde{\gamma}_{\xi}^{e'} \tag{27}$$

where $\mathbf{J}$ is the Jacobian matrix that entails the correspondence between the shear strain in the physical coordinate system, $\widetilde{\gamma}_{xy}$, and its representation in the natural coordinate system, $\widetilde{\gamma}_{\xi}$.

The shear strain field $\widetilde{\gamma}_{\xi}^{e'}$ in Equation (27) is represented by a $(p-1)$ order polynomial:

$$\widetilde{\gamma}_{\xi}^{e'} = a_0 + a_1\xi + a_2\xi^2 + \cdots + a_{p-1}\xi^{p-1} = \boldsymbol{\xi}\mathbf{a} \tag{28}$$

where $\mathbf{a}$ is a vector that collects the polynomial coefficients a_0, a_1, a_2, $\ldots$, a_{p-1}. These coefficients are obtained from the solution of a linear system of p equations from the evaluation of Equation (28) at the internal points ξ':

$$\begin{pmatrix} \widetilde{\gamma}_{\xi}^{e'}(\xi'_1) \\ \widetilde{\gamma}_{\xi}^{e'}(\xi'_2) \\ \vdots \\ \widetilde{\gamma}_{\xi}^{e'}(\xi'_p) \end{pmatrix} = \begin{bmatrix} 1 & \xi'_1 & \xi_1^{2'} & \ldots & \xi_1^{p-1'} \\ 1 & \xi'_2 & \xi_2^{2'} & \ldots & \xi_2^{p-1'} \\ \vdots & & & \ddots & \\ 1 & \xi'_p & \xi_p^{2'} & \ldots & \xi_p^{p-1'} \end{bmatrix} \begin{pmatrix} a_0 \\ a_1 \\ \vdots \\ a_{p-1} \end{pmatrix} = \mathbf{Pa} \tag{29}$$

The polynomial coefficients can be obtained from the strain $\widetilde{\gamma}_\xi^{e'}$ using a similar approximation to those defined by Equation (19) but in natural coordinates:

$$\mathbf{a} = \mathbf{P}^{-1}\widetilde{\gamma}_\xi^{e'} = \mathbf{P}^{-1}\sum_{i=1}^{p+1}\mathbf{B}_{\gamma 0}^{i}(\xi_i')\widetilde{\mathbf{u}}_s^{e,i} \tag{30}$$

Finally, substituting Equations (28) and (30) into Equation (27) yields:

$$\widetilde{\gamma}_{xy}^{e} = \mathbf{J}^{-1}\boldsymbol{\xi}\mathbf{P}^{-1}\sum_{i=1}^{p+1}\mathbf{B}_{\gamma 0}^{i}(\xi')\widetilde{\mathbf{u}}_s^{e,i} = \sum_{i=1}^{p+1}\left[\mathbf{B}_{\gamma 0}^{i'}\right]\widetilde{\mathbf{u}}_s^{e,i} = \mathbf{B}_{\gamma 0}^{e'}\widetilde{\mathbf{u}}_s^{e} \tag{31}$$

where $\mathbf{B}_{\gamma 0}^{e'}$ is the substitute transverse shear strain matrix used to computed the stiffness matrix $\mathbf{K}_{\gamma 0}^{e}$:

$$\mathbf{K}_{\gamma 0}^{e} = \int_{A_s^e}\left[\mathbf{B}_{\gamma 0}{}^{e'T} C_\gamma \mathbf{B}_{\gamma 0}^{e'}\right] dA \tag{32}$$

The proposed stabilisation method is quite straightforward and it is only required the computation of the substitutive matrix $\mathbf{B}_{\gamma 0}^{e'}$. This procedure results in a free shear locking plate element based on the Reissner-Mindlin and the Kirchhoff-Love formulations.

The nodal element coordinates define an orthogonal basis. Then, the element matrices $\mathbf{M}^e$ and $\mathbf{K}_{\chi 4}^{e}$ are easily computed as follows:

$$\mathbf{M}^e(k,l) = \delta_{ij}\rho_s t w_i |\mathbf{J}(\xi_i)|\,, \tag{33}$$

$$\mathbf{M}^e(k,l+1) = \delta_{ij}\frac{\rho_s t^3}{12} w_i |\mathbf{J}(\xi_i)|\,, \tag{34}$$

$$\mathbf{K}_{\chi 4}^{e}(k,l) = \delta_{ij}\frac{E t^3}{12(1-\nu^2)} w_i |\mathbf{J}(\xi_i)|\,, \tag{35}$$

$$\text{with}\quad k = 2(i-1)+1\,,\quad l = 2(j-1)+1$$

$$\text{and}\quad i,j = 1,\ldots,p+1$$

where δ_{ij} is the Kronecker delta, w_i is the LGL weight at the natural nodal coordinate ξ_i and $|\mathbf{J}(\xi_i)|$ is the Jacobian evaluated at ξ_i.

The element stiffness matrices $\mathbf{K}_{\chi 0}^{e}$, $\mathbf{K}_{\chi 2}^{e}$ and $\mathbf{K}_{\gamma 0}^{e}$ are numerically integrated with a LGL quadrature of the same order than the element approximation p. Moreover, it can be easily proved that the stiffness matrices $\mathbf{K}_{\chi 1}^{e}$ and $\mathbf{K}_{\chi 3}^{e}$ are identically null.

2.2. The 2.5D spectral element method in fluid-acoustics

The wave propagation within an inviscid fluid is expressed by the homogeneous Helmholtz equation [56]. The 2.5D governing equation in fluid acoustics is derived from the 3D formulation assuming that the fluid subdomain is invariant in the longitudinal direction [11]. The solution to the 3D problem can be written as the superposition of 2D solutions with different longitudinal wavenumbers k_z taking into account the Fourier decomposition defined by Equation (3):

$$\nabla^2\left(\widetilde{p}e^{-ik_z z}\right)+k_f^2\widetilde{p}e^{-ik_z z}=0 \tag{36}$$

where $k_f=\omega/c_f$ is the fluid wavenumber and $\widetilde{p}$ is the fluid pressure in the frequency-wavenumber domain. The finite element equation is derived from a consistent field of pressure $\delta\widetilde{p}$ acting over the subdomain Ω_f:

$$\int_{\Omega_f}\delta\widetilde{p}\nabla^2\left(\widetilde{p}e^{-ik_z z}\right)d\Omega+k_f^2\int_{\Omega_f}\delta\widetilde{p}\,\widetilde{p}e^{-ik_z z}\,d\Omega=0 \tag{37}$$

The fluid weak formulation is addressed applying the Green's theorem to Equation (37) and using the fluid momentum equation relating the pressure and the displacement particle, $\widetilde{\mathbf{u}}_f$, at the fluid boundary Γ_f: $\nabla\widetilde{p}=-\omega^2\rho_f\widetilde{\mathbf{u}}_f$. The virtual work expression defined by Equation (37) yields:

$$\begin{aligned}&-k_f^2\int_{\Omega_f}\delta\widetilde{p}\,\widetilde{p}e^{-ik_z z}\,d\Omega+\int_{\Omega_f}\nabla(\delta\widetilde{p})^T\nabla\left(\widetilde{p}e^{-ik_z z}\right)d\Omega+\omega^2\rho_f\int_{\Gamma_f}\delta\widetilde{p}\mathbf{n}_f^T\widetilde{\mathbf{u}}_f e^{-ik_z z}\,d\Gamma\\&-\int_{\Gamma_f}\delta\widetilde{p}\,\widetilde{p}\nabla\left(e^{-ik_z z}\right)^T\mathbf{n}_f\,d\Gamma=0\end{aligned} \tag{38}$$

where $\mathbf{n}_f$ is the outward normal vector at the fluid boundary Γ_f.

The last term of the left-hand member in Equation (38) is computed by making use again of the Green's theorem:

$$\begin{aligned}&\int_{\Gamma_f}\delta\widetilde{p}\,\widetilde{p}\nabla\left(e^{-ik_z z}\right)^T\mathbf{n}_f\,d\Gamma=\int_{\Omega_f}\delta\widetilde{p}\,\widetilde{p}\nabla^2\left(e^{-ik_z z}\right)d\Omega+\int_{\Omega_f}\nabla\left(\delta\widetilde{p}\,\widetilde{p}\right)^T\nabla\left(e^{-ik_z z}\right)d\Omega=\\&-k_z^2\int_{\Omega_f}\delta\widetilde{p}\,\widetilde{p}e^{-ik_z z}\,d\Omega+\int_{\Omega_f}\left(\delta\widetilde{p}\nabla(\widetilde{p})+\widetilde{p}\nabla\left(\delta\widetilde{p}\right)\right)^T\nabla\left(e^{-ik_z z}\right)d\Omega\end{aligned} \tag{39}$$

Then, substituting Equation (39) into Equation (38):

$$\begin{aligned}&-\widetilde{k}_f^2\int_{\Omega_f}\delta\widetilde{p}\,\widetilde{p}e^{-ik_z z}\,d\Omega+\int_{\Omega_f}\nabla(\delta\widetilde{p})^T\nabla\left(\widetilde{p}e^{-ik_z z}\right)d\Omega+\omega^2\rho_f\int_{\Gamma_f}\delta\widetilde{p}\mathbf{n}_f^T\widetilde{\mathbf{u}}_f e^{-ik_z z}\,d\Gamma\\&-\int_{\Omega_f}\left(\delta\widetilde{p}\nabla(\widetilde{p})+\widetilde{p}\nabla(\delta\widetilde{p})\right)^T\nabla\left(e^{-ik_z z}\right)d\Omega=0\end{aligned} \tag{40}$$

where $\widetilde{k}_f=\sqrt{k_f^2-k_z^2}$.

From the two directional vectors, $\mathbf{v}_1=[1\quad 1\quad 0]^T$ and $\mathbf{v}_2=[0\quad 0\quad 1]^T$, and expanding the gradient of products, Equation (40) can be written as:

$$\begin{aligned}&-\widetilde{k}_f^2\int_{\Omega_f}\delta\widetilde{p}\,\widetilde{p}e^{-ik_z z}\,d\Omega+\int_{\Omega_f}\nabla_{\mathbf{v}_1}(\delta\widetilde{p})^T\left(\nabla_{\mathbf{v}_1}(\widetilde{p})e^{-ik_z z}+\widetilde{p}\nabla_{\mathbf{v}_2}(e^{-ik_z z})\right)d\Omega\\&+\omega^2\rho_f\int_{\Gamma_f}\delta\widetilde{p}\mathbf{n}_f^T\widetilde{\mathbf{u}}_f e^{-ik_z z}\,d\Gamma-\int_{\Omega_f}\left(\delta\widetilde{p}\nabla_{\mathbf{v}_1}(\widetilde{p})+\widetilde{p}\nabla_{\mathbf{v}_1}(\delta\widetilde{p})\right)^T\nabla_{\mathbf{v}_2}(e^{-ik_z z})\,d\Omega=0\end{aligned} \tag{41}$$

Equation (41) can be simplified considering that the cross product of directional derivatives defined by the operators $\nabla_{\mathbf{v}_1}$ and $\nabla_{\mathbf{v}_2}$ vanishes due to the orthogonality of the vectors $\mathbf{v}_1$ and $\mathbf{v}_2$:

$$-\widetilde{k}_f^2 \int_{\Omega_f} \delta\widetilde{p}\,\widetilde{p} e^{-ik_z z}\, d\Omega + \int_{\Omega_f} \nabla_{\mathbf{v}_1}(\delta\widetilde{p})^T \nabla_{\mathbf{v}_1}(\widetilde{p}) e^{-ik_z z}\, d\Omega + \omega^2 \rho_f \int_{\Gamma_f} \delta\widetilde{p}\mathbf{n}_f^T \widetilde{\mathbf{u}}_f e^{-ik_z z}\, d\Gamma = 0 \tag{42}$$

Equation (42) is expressed in a simpler form assuming invariant longitudinal geometry:

$$-\widetilde{k}_f^2 \int_{A_f} \delta\widetilde{p}\,\widetilde{p}\, dA + \int_{A_f} \nabla_{\mathbf{v}_1}(\delta\widetilde{p})^T \nabla_{\mathbf{v}_1}(\widetilde{p})\, dA + \omega^2 \rho_f \int_{\Sigma_f} \delta\widetilde{p}\mathbf{n}_f^T \widetilde{\mathbf{u}}_f\, d\Sigma = 0 \tag{43}$$

where A_f is the cross section of the fluid subdomain and Σ_f is the boundary of this section.

The fluid subdomain is discretised into elements of order p. The pressure and the displacement particle vector within an element are approximated using the element shape functions $\mathbf{N}$ and $\boldsymbol{\phi}$, respectively as:

$$\sum_{i=1}^{p+1}\sum_{j=1}^{p+1} \mathbf{N}^{ij}\widetilde{p}^{ij} = \mathbf{N}^e \widetilde{p}^e \tag{44}$$

$$\sum_{i=1}^{p+1} \phi^i \widetilde{\mathbf{u}}_f^i = \boldsymbol{\phi}\widetilde{\mathbf{u}}_f^e \tag{45}$$

Thus, Equation (43) for an element is rewritten as follows:

$$-\widetilde{k}_f^2 \int_{A_f^e} \delta\widetilde{p}^e \mathbf{N}^{e^T} \mathbf{N}^e \widetilde{p}^e\, dA + \int_{A_f^e} \delta\widetilde{p}^e \left(\nabla_{\mathbf{v}_1}\mathbf{N}^e\right)^T \left(\nabla_{\mathbf{v}_1}\mathbf{N}^e\right) \widetilde{p}^e\, dA + \omega^2 \rho_f \int_{\Sigma_f^e} \delta\widetilde{p}^e \mathbf{N}^{e^T} \mathbf{n}_f^{e^T} \boldsymbol{\phi}\widetilde{\mathbf{u}}_f^e\, d\Sigma = 0 \tag{46}$$

Then, the 2.5D fluid governing equation is addressed through elimination of the pressure $\delta\widetilde{p}$. The following expression is obtained defining matrices $\mathbf{D}^e$, $\mathbf{F}^e$ and $\mathbf{R}^e$:

$$\left[-\widetilde{k}_f^2 \mathbf{D}^e + \mathbf{F}^e\right] \widetilde{p}^e = -\omega^2 \rho_f \mathbf{R}^e \widetilde{\mathbf{u}}_f^e \tag{47}$$

Finally, Equation (47) is evaluated for elements in the fluid subdomain and Equation (43) can be rewritten considering assembled global matrices $\mathbf{D}$, $\mathbf{F}$ and $\mathbf{R}$:

$$\widetilde{\mathbf{F}}\widetilde{p} = -\omega^2 \rho_f \mathbf{R}\widetilde{\mathbf{u}}_f \tag{48}$$

where the fluid dynamic matrix $\widetilde{\mathbf{F}} = -\widetilde{k}_f^2 \mathbf{D} + \mathbf{F}$ is computed for each wavenumber.

The computation of matrix $\widetilde{\mathbf{F}}$ requires the discretisation of the integration region A_f into elements. LGL polynomials of order p are used in the proposed method as shape functions $\mathbf{N}$ for both geometry and pressure approximations. The nodes in natural coordinates $(\xi, \eta) \in [-1, 1] \times [-1, 1]$ are at the LGL points:

$$\begin{cases} (1-\xi^2)\dfrac{\partial \mathbf{N}(\xi,\eta)}{\partial \xi} = 0 \\ (1-\eta^2)\dfrac{\partial \mathbf{N}(\xi,\eta)}{\partial \eta} = 0 \end{cases} \tag{49}$$

The nodal element coordinates define an orthogonal basis as they coincide with the LGL integration points. Then, the fluid element matrices are easily computed as follows:

$$\mathbf{D}^e(i,j) = \delta_{ij} w_{ij} |\mathbf{J}(\xi_i,\eta_j)| \,, \tag{50}$$

$$\mathbf{R}^e(i,k) = \delta_{ij} \mathbf{n}_f^e(l) w_i' |\mathbf{J}'(\xi_i)| \,, \tag{51}$$

$$\text{with} \quad i,j = 1,\ldots,p+1$$

$$\text{and} \quad k = 2(i-1)+l \,, \quad l = 1,2$$

In Equation (50), δ_{ij} is the Kronecker delta, w_{ij} is the LGL weight at the natural nodal coordinates (ξ_i, η_j) and $|\mathbf{J}(\xi_i,\eta_j)|$ is the Jacobian evaluated at (ξ_i, η_j). Equation (51) is only defined for nodes belonging to Γ_f with Neumann boundary conditions. Here, w_i' is the LGL weight at the nodal coordinate ξ_i, $|\mathbf{J}'(\xi_i)|$ is the Jacobian computed from the shape function ϕ^i and the boundary geometry, and $\mathbf{n}_f^e(l)$ is the l-th component of the outward normal vector to A_f^e. The element fluid matrix $\mathbf{F}^e$ is numerically integrated with a LGL quadrature of order p.

The fluid subdomain Ω_f is discretised into elements with one degree of freedom per node, representing pressure. The element definition is done by using a polynomial interpolation $\mathbf{L}$ defined from an element base mesh $\mathbf{x}$ with n points and its representation in the natural coordinate system. The element nodal coordinates are obtained as $\mathbf{x}_i = \sum_{k=1}^{n} \mathbf{L}_k(\xi_i,\eta_i)\mathbf{x}_k$. As an example, Figure 5 shows a $p=6$ element generated from a base mesh with $n=9$ points for the approximation of the element geometry.

The element shape functions are computed as $\mathbf{N}^k(\xi,\eta) = \phi^i(\xi)\phi^j(\eta)$; being ϕ^i and ϕ^j one-dimensional LGL shape functions defined by Equation (25), and $k = (i-1)(p+1)+j$ the related element node. The shape functions $\mathbf{N}^e$ and its derivatives are symbolically computed in a straightforward procedure for an arbitrary element order. Figure 6 shows the interpolation shape functions $\mathbf{N}^{25}$ and $\mathbf{N}^{41}$ for the spectral element presented in Figure 5 ($p=6$).

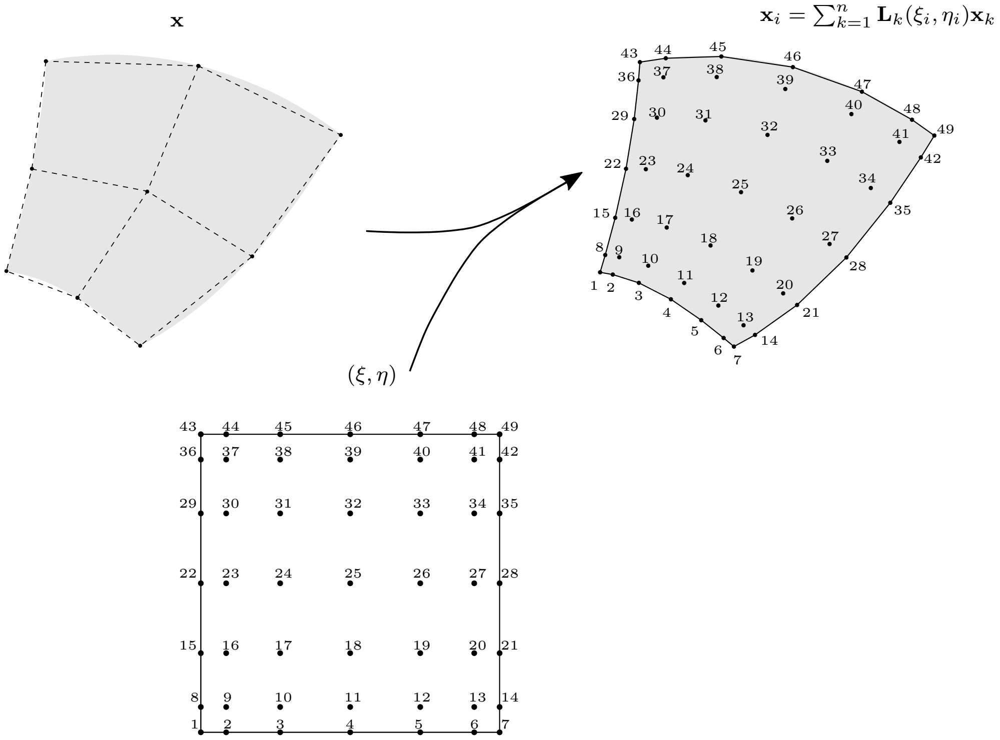

Figure 5: Base element mesh and natural coordinate system used to obtain the physical representation of a spectral element of order $p = 6$.

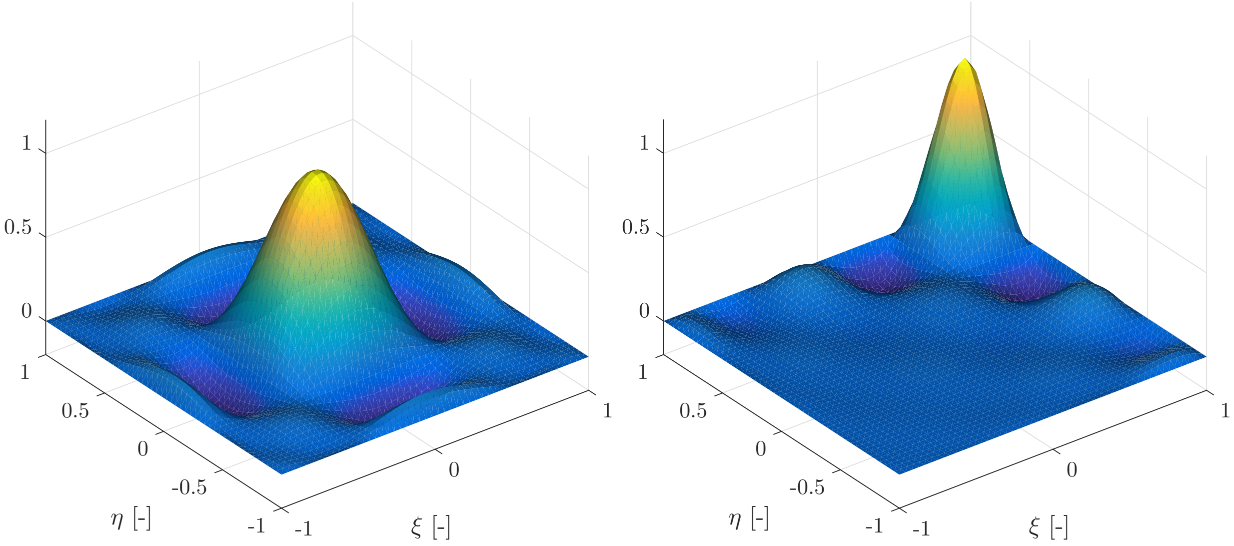

(a) (b)

Figure 6: Element shape functions (a) $\mathbf{N}^{25}$ and (b) $\mathbf{N}^{41}$ for a fluid spectral element with order $p = 6$.

2.3. Fluid-solid coupling procedure

Equations (23) and (48) are coupled imposing equilibrium of normal pressure, null shear stresses and compatibility of displacement at the interface Γ_f. Both equations are assembled into a single comprehensive system, together with the equilibrium and compatibility conditions.

The load vector $\widetilde{\mathbf{f}}_q$ at the solid-fluid interface is obtained by integrating the fluid pressure field $\widetilde{p}_q$ in Γ_q:

$$\widetilde{\mathbf{f}}_q = -\int_{\Gamma_q} \phi^T \mathbf{n}_{sq} \mathbf{N} \widetilde{p}_q \, d\Gamma = -\mathbf{R}^T \widetilde{p}_q \tag{52}$$

Substituting Equation (52) into Equation (23), the following system of equations is defined according to the subdomain decomposition:

$$\begin{bmatrix} \widetilde{\mathbf{K}}_{ss} & \widetilde{\mathbf{K}}_{sq} \\ \widetilde{\mathbf{K}}_{qs} & \widetilde{\mathbf{K}}_{qq} \end{bmatrix} \begin{bmatrix} \widetilde{\mathbf{u}}_s \\ \widetilde{\mathbf{u}}_q \end{bmatrix} = \begin{bmatrix} \widetilde{\mathbf{f}}_s \\ -\mathbf{R}^T \widetilde{p}_q \end{bmatrix} \tag{53}$$

where the subscript q indicates degrees of freedom belonging to Γ_q and s stands for the rest of structural degrees of freedom.

Analogously, the fluid governing expression (Equation (48)) is split into two parts:

$$\begin{bmatrix} \widetilde{\mathbf{F}}_{qq} & \widetilde{\mathbf{F}}_{qf} \\ \widetilde{\mathbf{F}}_{fq} & \widetilde{\mathbf{F}}_{ff} \end{bmatrix} \begin{bmatrix} \widetilde{p}_q \\ \widetilde{p}_f \end{bmatrix} = \begin{bmatrix} -\omega^2 \rho_f \mathbf{R} \widetilde{\mathbf{u}}_q \\ \mathbf{0} \end{bmatrix} \tag{54}$$

where the subscript q indicates degrees of freedom shared with the structural subdomain and f stands for the rest of fluid degrees of freedom.

Finally, the coupling of Equations (53) and (54) is carried out with the imposition of equilibrium and compatibility conditions at the interface Γ_q. Both systems of equations are assembled into an overall system:

$$\begin{bmatrix} \widetilde{\mathbf{K}}_{ss} & \widetilde{\mathbf{K}}_{sq} & \mathbf{0} & \mathbf{0} \\ \widetilde{\mathbf{K}}_{qs} & \widetilde{\mathbf{K}}_{qq} & \mathbf{R}^T & \mathbf{0} \\ \mathbf{0} & \omega^2 \rho_f \mathbf{R} & \widetilde{\mathbf{F}}_{qq} & \widetilde{\mathbf{F}}_{qf} \\ \mathbf{0} & \mathbf{0} & \widetilde{\mathbf{F}}_{fq} & \widetilde{\mathbf{F}}_{ff} \end{bmatrix} \begin{bmatrix} \widetilde{\mathbf{u}}_s \\ \widetilde{\mathbf{u}}_q \\ \widetilde{p}_s \\ \widetilde{p}_f \end{bmatrix} = \begin{bmatrix} \widetilde{\mathbf{f}}_s \\ \mathbf{0} \\ \mathbf{0} \\ \mathbf{0} \end{bmatrix} \tag{55}$$

Equation (55) is solved in the frequency-wavenumber domain to compute the coupled fluid-solid response.

3. Numerical verification

The proposed method was verified with benchmark problems that study the wave propagation in elastic and acoustic waveguides. The numerical results were compared with reference solutions and the L_2 scaled error, ϵ_2, was used to assess the accuracy [26]:

$$\epsilon_2 = \frac{||f_{ex} - f_h||}{||f_{ex}||} \tag{56}$$

where f_{ex} denotes the reference solution and f_h is the result computed by the proposed methodology. The scaled L_2 error ϵ_2 is generally used to measure the pollution effect at high wavenumbers [26, 57].

Different $h-p$ strategies were investigated to get the optimal discretisation with the lowest computational effort. The nodal density per wavelength is used to describe the mesh density [58]:

$$d_\lambda = \frac{2\pi p}{hk^*} \tag{57}$$

where k^* is a characteristic wavenumber, h is the element length and p is the order of the shape functions.

The benchmark problems presented herein were solved in a computer with an Intel Core i7-6600 processor at 2.6 GHz. The transpose-free quasi-minimal residual method (TFQMR) together with an ILU preconditioner were employed to solve the resulting system of equations.

3.1. Solid waveguide

The proposed spectral element for plate structures was verified studying the response of a lightened aluminium clamped plate with a width $W = 10\,\mathrm{m}$. The plate thickness was set to $t = 0.1\,\mathrm{m}$, leading to a slenderness ratio $W/t = 100$ which is in accordance to very thin plate behaviour. The structure was vertically loaded by a harmonic force acting at $x = W/2$. The material properties were: Young's modulus $E = 70 \times 10^9\,\mathrm{N/m^2}$, Poisson's ratio $\nu = 0.25$ and density $\rho = 100\,\mathrm{kg/m^3}$.

The accuracy of the proposed element was tested against a thin-shell finite element approach [7]. The problem solution was computed in the frequency domain up to 700 Hz, considering a longitudinal wavenumber $k_z = 0.4\,\mathrm{rad/m}$. A SEM discretisation $(1/h, p) = (2, 4)$ allowed a nodal density $d_\lambda \geq 12$ for the plane-wave phase velocity $C_L = (D\omega^2/\rho t)^{0.25}$ in the slab [59, 60], where the bending stiffness was $D = Et^3/12(1-\nu^2)$. The FEM discretisation adequately represented the slab response using a similar nodal density as the SEM model. Figure 7 shows the vertical displacement at a point located at $x = W/2$ in the frequency range from 0 to 700 Hz. The structural response showed peaks at the resonance frequencies, where the proposed solution slightly differed with regard to FEM since the problem became ill conditioned. Nevertheless, it can be concluded that the spectral element reproduced adequately the plate behaviour even for a very thin plate. The shear locking did not appear in the proposed element formulation as it occurs if an 2.5D element based on Reissner-Mindlin formulation is considered. Moreover, it should be mentioned that the element did not present any problem when thick plates were studied.

Next, the scaled L_2 error ϵ_2 was computed for different $h-p$ discretisations. A convergence study was done in order to obtain a reference result from the proposed model since it does not exist any analytical solution for the analysed problem. Four discretisations were considered with characteristic element size given by $1/h = \{0.2,\ 0.4,\ 1,\ 2\}\,\mathrm{m}^{-1}$. The element order p varied from 1 to 15. Figure 8.(a) shows the convergence of the vertical displacement at $x = W/2$ for an excitation frequency of 700 Hz. The solution converged to $u_y = 2.66 \times 10^{-8}\,\mathrm{m}$ for an adequate element order. The scaled L_2 error ϵ_2 is represented in Figure

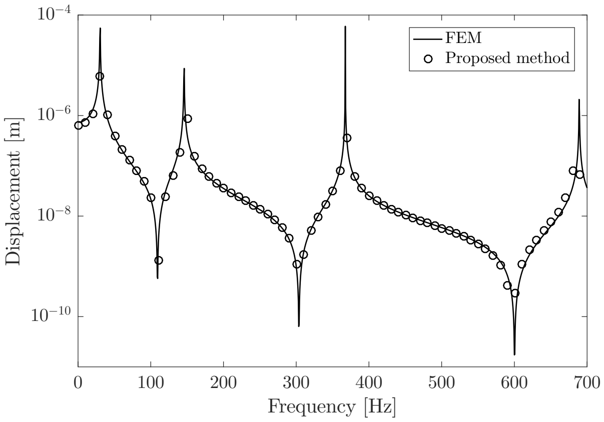

Figure 7: Vertical displacement at $x = W/2$ computed with the proposed method and the FEM [7].

8.(b) using this value as the reference for each discretisation. For finer discretisations, the error decayed monotonically resulting in faster convergence. However, the coarser meshes $1/h = \{0.2,\, 0.4\}\,\mathrm{m}^{-1}$ did not present a monotonic decay due to their element size was not enough to properly compute the solution. Therefore, low nodal densities per wavelength, d_λ, discretisations did not represent accurately the problem to be solved. The minimum error was $\epsilon_2 \approx 10^{-11}$. The lowest nodal densities to reach this error were $d_\lambda = 13$ for $(1/h, p) = (0.4, 12)$, $d_\lambda = 24$ for $(1/h, p) = (1, 9)$, and $d_\lambda = 37$ for $(1/h, p) = (2, 7)$. The coarsest mesh presented a minimum error $\epsilon_2 \approx 10^{-8}$ when $d_\lambda = 8$ and $p = 15$. The computational CPU time increased linearly with the element order, slightly affected by the problem discretisation (Figure 8.(c)). Finer discretisations were more efficient than coarser meshes as they needed less computational effort for a desirable error (Figure 8.(d)).

In some cases, a coarser mesh with lower nodal density could be required to compute the problem solution with lower nodal density ensuring an acceptable accuracy. Table 2 shows typical discretisations to obtain an error $\epsilon_2 \leq 10^{-3}$. It should be noticed that the nodal densities were higher as the element size decreased since d_λ is proportional to $1/h$. The results conclude that a minimum nodal density $d_\lambda = 6$ allowed to approximate the problem solution with the indicated accuracy.

Table 2: Summary of nodal density (d_λ), total number of degrees of freedom (DOF) and CPU time for different spectral $h-p$ discretisations to approximate the problem solution at excitation frequency 700 Hz with the accepted accuracy $\epsilon_2 \leq 10^{-3}$.

$1/h$ [m^{-1}]	p [-]	d_λ [-]	DOF [-]	CPU [s]
0.2	12	6	50	2.969×10^{-3}
0.4	8	8	66	2.016×10^{-3}
1	5	13	102	1.326×10^{-3}
2	4	21	162	1.154×10^{-3}

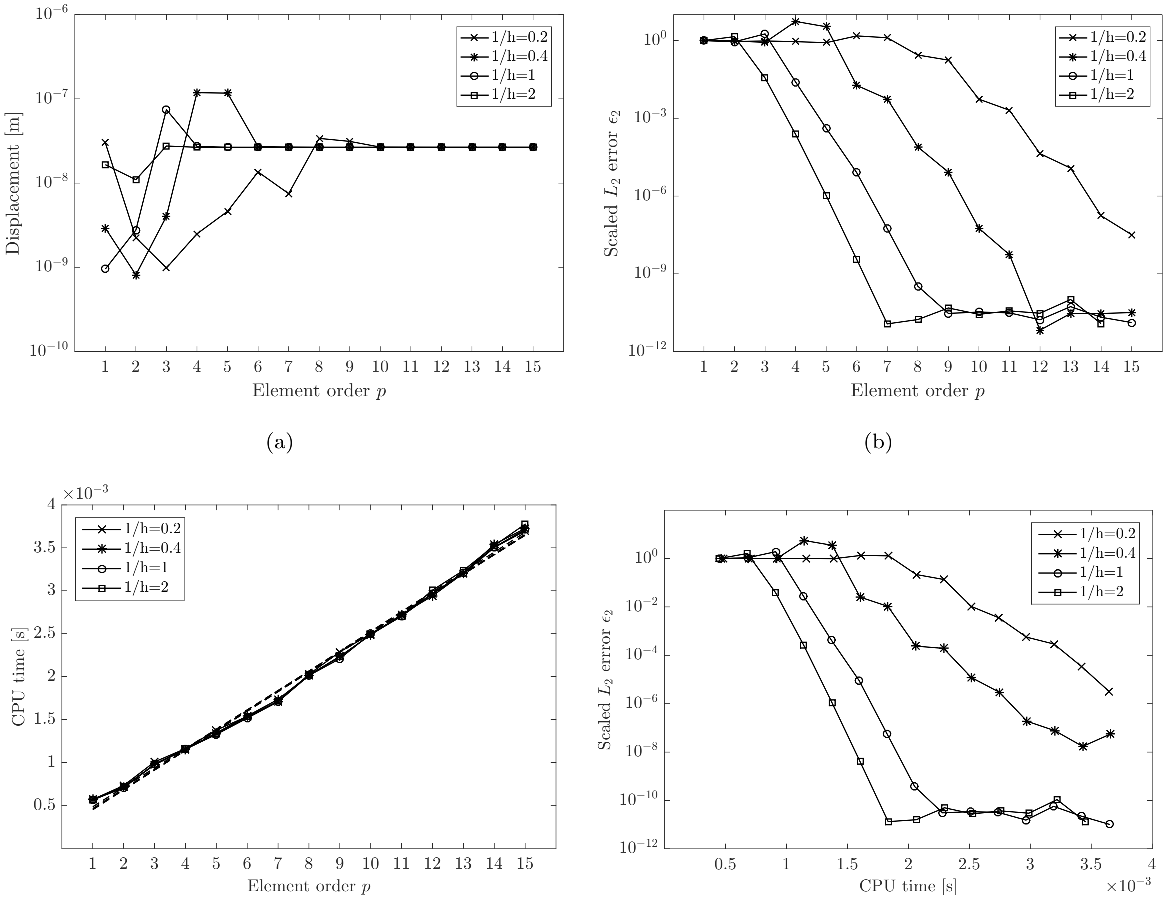

(a) (b)

(c) (d)

Figure 8: (a) Convergence of vertical displacement at $x = W/2$ for an excitation frequency 700 Hz, (b) scaled L_2 error ϵ_2, (c) CPU time and (d) scaled L_2 error ϵ_2 versus CPU time for different discretisations $1/h$ and element polynomial orders p.

Finally, it can be concluded that the scaled L_2 error ϵ_2 was not affected by the longitudinal wavenumber k_z. Equation (22) states that the integration of element matrices does not depend on the longitudinal wavenumber, so the accuracy of the method was not constrained by k_z.

3.2. Fluid waveguide

This section analyses the feasibility of the proposed spectral element to study fluid acoustic problems. The example concerned a rectangular fluid waveguide with a width $W = 3\,\mathrm{m}$ and a height $H = 2\,\mathrm{m}$ (Figure 9). The fluid had air properties with density $\rho_f = 1.225\,\mathrm{kg/m^3}$ and dilatational wave propagation velocity $c_f = 340\,\mathrm{m/s}$. The left side had null pressure while the opposite one was subjected to an uniform normal velocity $v_n = 1\,\mathrm{m/s}$. All the remaining boundaries had velocity constraint $v_n = 0\,\mathrm{m/s}$. This problem has analytical solution for the one-dimensional case, i.e. $k_z = 0$ [27]:

$$p(x, \omega) = \frac{1}{k_f} i \rho_f \omega \frac{\sin(k_f x)}{\cos(k_f W)} \tag{58}$$

Firstly, the problem solution was computed for a harmonic source with frequency 1000 Hz and $k_z = 0$. Four different domain discretisations were investigated with characteristic element sizes $1/h = \{1, 2, 4, 8\}\,\mathrm{m}^{-1}$ (Figure 10). Element order p varied from 1 to 15.

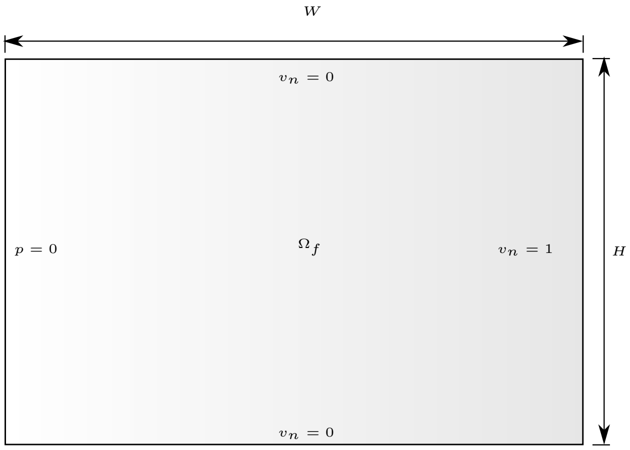

Figure 9: Fluid waveguide definition

The accuracy of computed results was again evaluated using the scaled L_2 error ϵ_2 (Equation (56)) over the fluid domain [26] using the analytical solution as reference. Figure 11 represents the error, the total number of degree of freedom, the CPU time and the error versus the CPU time for different $h - p$ configurations. The problem convergence started with an initial value $\epsilon_2 = 1$ for $p = 1$ and decreased for a certain element order depending on the mesh discretisation [17]. From this order, the curves showed an exponentially monotonic convergence with the element order p. For the finest mesh, $1/h = 8$, the error did not decrease with the increment of the element order from $p = 13$ because of the systems of equations for this dense mesh and high-order approximations were ill conditioned as it was described in References [26, 61]. Regarding the nodal density d_λ, it was found that it increased linearly with the element order according to Equation (57), while the total number of degrees of freedom did it quadratically for 2D discretisations. Figure 11.(c) represents the CPU time for the computation and assembly of elements matrices. The CPU time was found adjusted to $e^{0.5p}$ for the studied discretisations. Medium size discretisations presented the lowest computational effort for a moderate error level (Figure 11.(d)). However, the finest mesh became more efficient as the required error decreased because of a lower element order was then needed.

The next issue concerned the identification of an adequate $h - p$ discretisation to solve this problem accurately with low CPU time consuming. Again, an error $\epsilon_2 \leq 10^{-3}$ was considered as an acceptable level of accuracy. The coarsest mesh ($1/h = 1\,\mathrm{m}^{-1}$) produced accurate results for an element order $p = 15$.

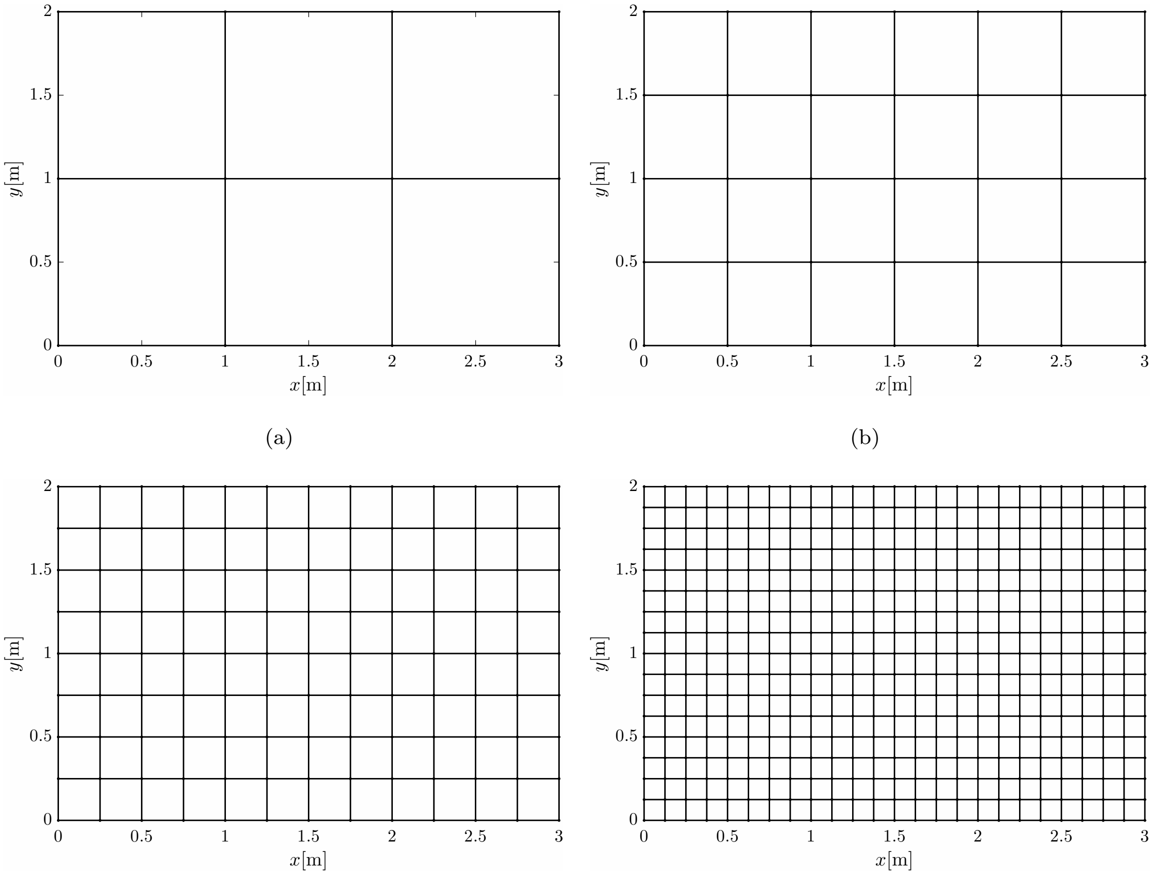

(a) (b) (c) (d)

Figure 10: Fluid domain discretisations for different element size: (a) $1/h = 1\,\mathrm{m}^{-1}$, (b) $1/h = 2\,\mathrm{m}^{-1}$, (c) $1/h = 4\,\mathrm{m}^{-1}$ and (d) $1/h = 8\,\mathrm{m}^{-1}$.

However, using finer discretisations, good results were computed, i. e. errors below the admissible tolerance, with lower element order. Table 3 summarizes the nodal density per wavelength, the total number of degrees of freedom (DOF) and the CPU time for the optimal $h-p$ discretisation to reach the solution with the acceptable error (Figure 11). This table shows that the configuration $(1/h, p) = (2, 9)$ allowed the minimum computational effort for the given accuracy. Other $h-p$ pairs involved higher computational effort due to the increment of DOF or high order interpolation functions that required quite computational effort to obtain the fluid matrices.

Finally, the problem solution was computed for a frequency range from 2 Hz to 1024 Hz and $k_z = 0$ using the discretisation $(1/h, p) = (2, 9)$. Figure 12.(a) compares the analytical and the numerical solutions. The fluid response exhibited several resonances at frequencies f_n given by [27]:

$$f_n = (2n-1)\frac{c_f}{4W} \qquad n = 1, 2, \ldots \tag{59}$$

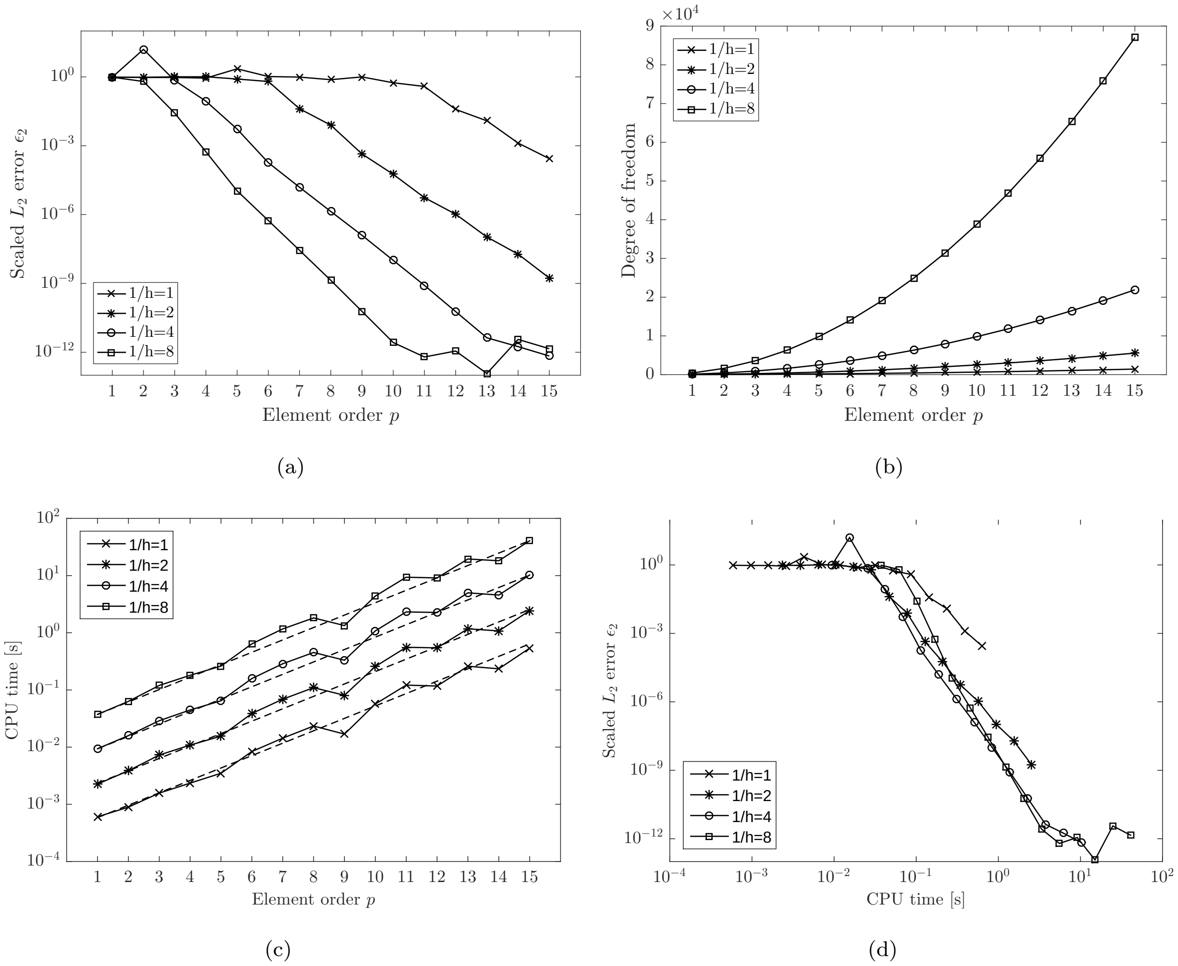

(a) (b)

(c) (d)

Figure 11: (a) Scaled L_2 error ϵ_2, (b) total number of degree of freedom, (c) CPU time and (d) scaled L_2 error ϵ_2 versus CPU time for different discretisations $1/h$ and element polynomial orders p.

Table 3: Summary of nodal density (d_λ), total number of degrees of freedom (DOF), and CPU time (CPU) for different spectral $h-p$ discretisations to approximate the problem solution with the accepted accuracy $\epsilon_2 \leq 10^{-3}$.

$1/h\,[\mathrm{m}^{-1}]$	p [-]	d_λ [-]	DOF [-]	CPU [s]
1	15	5	1426	5.387×10^{-1}
2	9	6	2035	8.065×10^{-2}
4	6	8	3577	1.582×10^{-1}
8	4	10	6305	1.803×10^{-1}

The accuracy of the proposed methodology was also evaluated from the solutions obtained with the $h-p$ pairs showed in Table 3. Figure 12.(b) shows the error ϵ_2 and the nodal density per wavelength. The minimum error oscillated around $\epsilon_2 = 10^{-14}$ for very high values of the nodal density d_λ. The error increased along the frequency range as the wavelength decreased. It is mentioned that several peaks appeared at the resonance frequencies where the problem was ill conditioned [26].

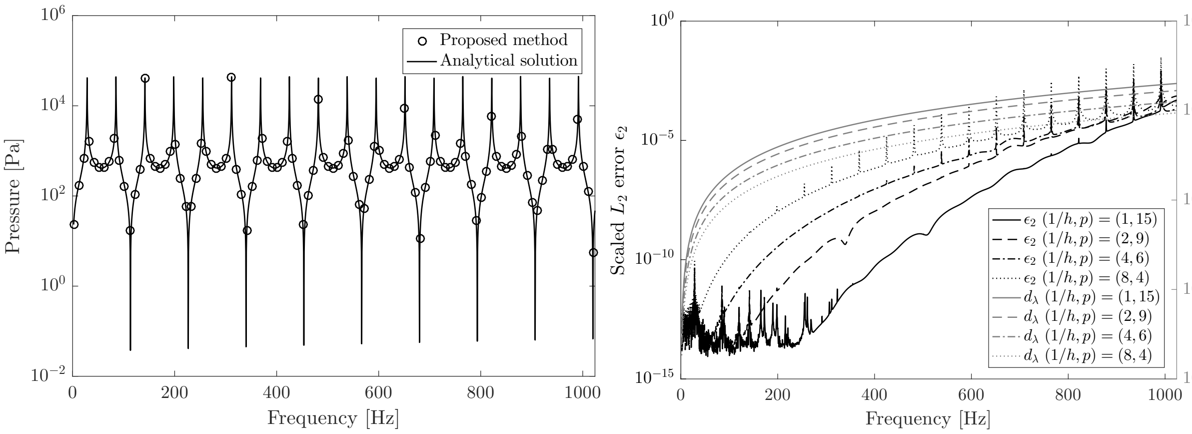

(a)

(b)

Figure 12: (a) Fluid pressure at $x = 1.5\,\mathrm{m}$ and $y = 1\,\mathrm{m}$ computed with the element order discretisation $(1/h, p) = (2, 9)$. (b) Scaled L_2 error ϵ_2 and nodal density per wave length d_λ for different $h - p$ discretisation.

The $h - p$ analysis concluded that the uniform p enrichment with a fixed mesh presented higher rates of convergence than the h refinement [62, 63]. Also, we found that a coarse mesh with a high element order produced accurate results with low computational effort when at least a nodal density per wavelength $d_\lambda = 6$ was ensured.

3.3. Rectangular duct with a flexible wall

In this section we studied the possibilities of the proposed methodology for studying fluid–structure interaction problems. The verification example represented an infinite cavity with one flexible side (Figure 13). At the remaining three sides, boundary conditions $v_n = 0\,\mathrm{m/s}$ were provided. The system dimensions were width $W = 0.106\,\mathrm{m}$ and height $H = 0.09\,\mathrm{m}$. The flexible plate was modelled as a clamped slab of thickness $t = 6 \times 10^{-3}\,\mathrm{m}$, Young modulus $E = 7.2 \times 10^{10}\,\mathrm{N/m^2}$, Poisson's ratio $\nu = 0.34$ and density $\rho = 2700\,\mathrm{kg/m^3}$. The fluid was air with density $\rho_f = 1.2\,\mathrm{kg/m^3}$ and sound propagation velocity $c_f = 344\,\mathrm{m/s}$. The problem discretisation was set to $h = 4\,\mathrm{m^{-1}}$ using an element order $p = 6$. Lawrie [3] presented the solution of this problem using a hybrid analytic-numerical method for modelling three-dimensional ducts of rectangular cross-section with flexible walls. The results computed by the proposed methodology were compared with the results from this semi-analytical approach.

The phase velocities of the FSI problem were computed to investigate the propagating modes of the system. Besides, the phase velocities were compared with those obtained from the structure and the fluid cavity neglecting the interaction between them. Figure 14 shows the phase velocities $C = \omega/k_z$. Here, the

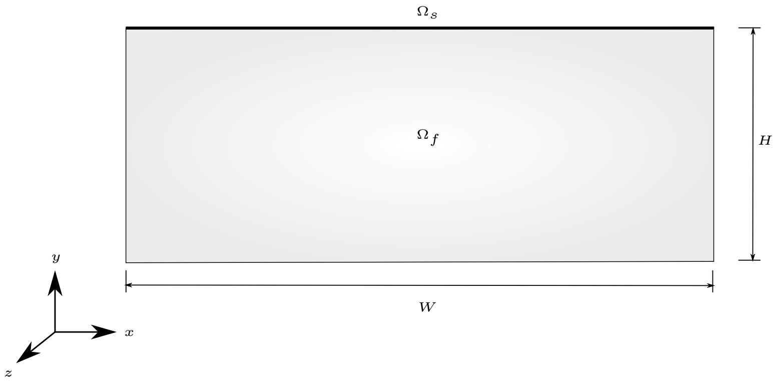

Figure 13: Rectangular duct with a flexible wall.

angular frequency ω was computed from an eigenvalue analysis of the equilibrium Equations (23), (48) and (55) for logarithmic spaced wavenumbers. The slab phase velocities (Figure 14.(a)) exhibited several cut-off frequencies which are in accordance with $f_n = 0.5\pi n^2 (EI/\overline{m}W^4)^{0.5}$, where $\overline{m} = \rho t = 1.62\,\mathrm{kg/m^2}$. Later, the waves became propagative and tended to the phase velocity C_L of the propagating plane waves in the slab [59]. The phase velocity curves were found to be dispersive over the entire frequency range.

On the other hand, the phase velocities for a rectangular acoustic waveguide with dimension $W \times H$ are given by $C_{mn} = c_f^2 \left((m\pi/k_z W)^2 + (n\pi/k_z H)^2 + 1\right)^{0.5}$, where C_{mn} is the phase velocity related to the propagating acoustic mode at the cut-off frequency $f_{mn} = c_f/2\pi((m\pi/W)^2 + (n\pi/H)^2)^{0.5}$. For the sake of simplicity, Figure 14.(b) only presents the phase velocity curves for the first five acoustic modes given by the frequencies $f_{00} = 0\,\mathrm{Hz}$, $f_{10} = 1623\,\mathrm{Hz}$, $f_{20} = 3245\,\mathrm{Hz}$, $f_{01} = 1911\,\mathrm{Hz}$ and $f_{11} = 2507\,\mathrm{Hz}$. The first acoustic mode had a non-dispersive phase velocity equals to the sound propagation velocity, c_f, while higher modes were dispersive with similar behaviour going to c_f above the cut-off frequency f_{mn}.

The phase velocities of the coupled problem provided the structural and the acoustic propagating modes. Figure 14.(c) presents three phase velocity curves. The propagation velocity of the first mode was close to the sound propagation velocity in the fluid at low frequencies and went to the plane wave phase velocity C_L of the slab as the frequency increased. The second mode exhibited a similar trend to that of the uncoupled slab around the cut-off frequency and became non-dispersive for high frequencies. Finally, the third mode was similar to the second one of the slab without interaction. Computed results were in accordance with the semi-analytical solution proposed by Lawrie [3]. The mismatches found in the Figure 14.(c) can be explained taking into account that the plate had a ratio $W/t = 17.6$ and it was modelled as a thin plate in Reference [3].

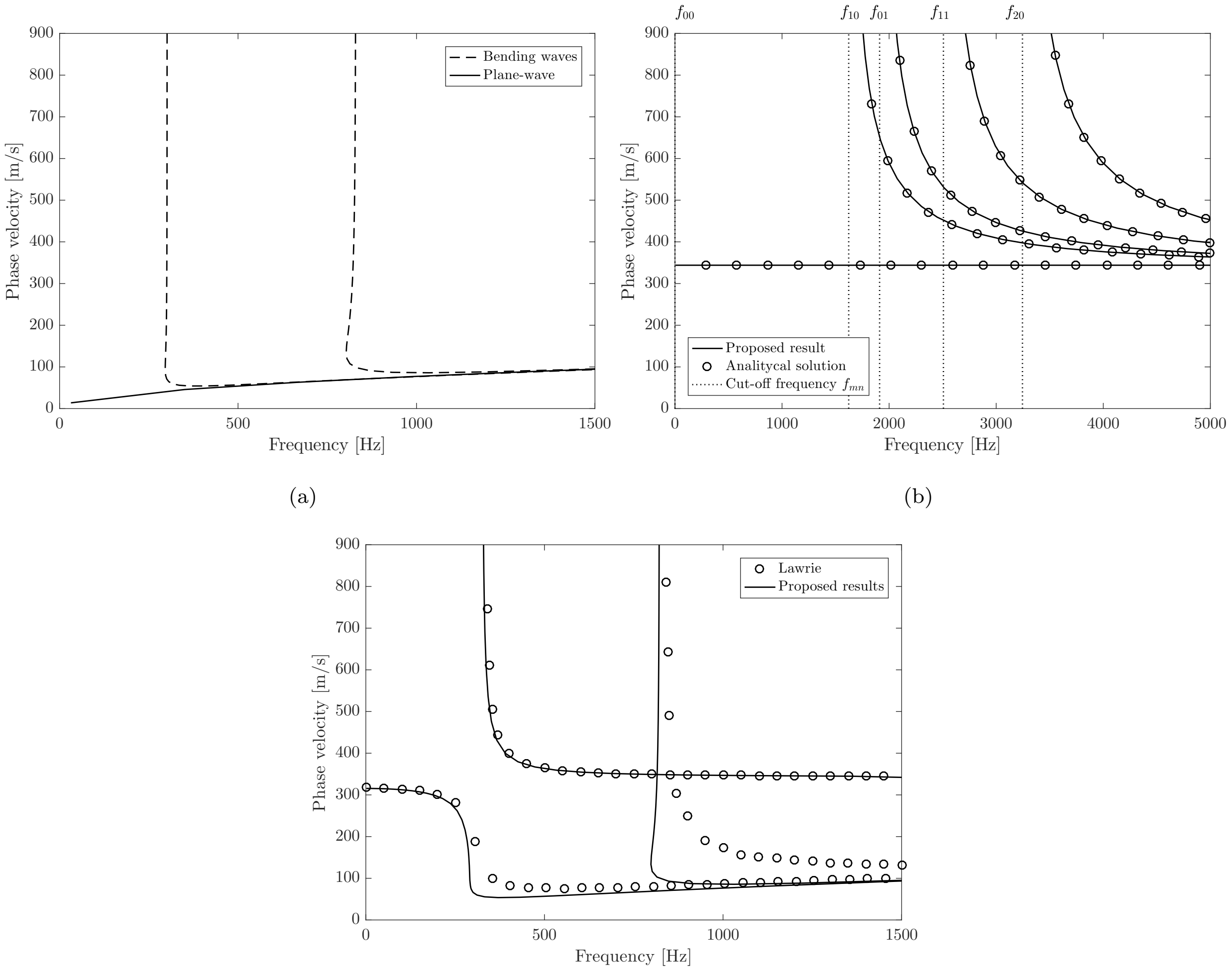

(a)

(b)

(c)

Figure 14: Phase velocity for (a) the structure, (b) the fluid and (c) the coupled fluid-structure system.

4. Numerical examples

In this section, two examples show the possibilities of the proposed methodology for studying fluid–structure interaction problems.

4.1. Acoustic cavity with a flexible side subjected to bending moment

The first example represented an infinite cavity with one flexible side subjected to a harmonic bending moment M (Figure 15). At the remaining three sides, boundary conditions $v_n = 0\,\mathrm{m/s}$ were provided. The system dimensions were width $W = 10\,\mathrm{m}$ and height $H = 4\,\mathrm{m}$.

This problem was firstly studied by Sandberg et al. [51] who computed the modes of the system. Later, Rodríguez-Tembleque et al. [52] analysed the fluid-structure response due to a harmonic bending moment

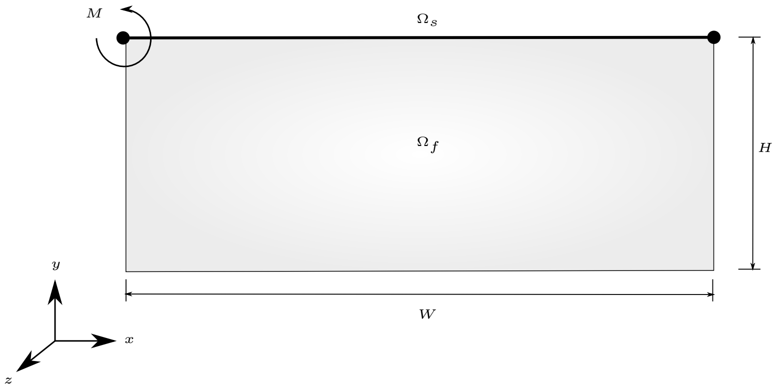

Figure 15: Acoustic cavity with a flexible side subjected to bending moment.

$M = M_0 e^{i\omega t}$ applied at one edge. Both analyses were done using a 2D formulation based on either a finite element formulation [51] or a coupled finite-boundary element formulation [52]. The cited authors modelled the structure as a beam with Young modulus $E = 2.1 \times 10^{11}\,\mathrm{N/m^2}$, Poisson's ratio $\nu = 0.3$, mass per unit length $\overline{m} = 50\,\mathrm{kg/m}$, cross section $A = 0.02\,\mathrm{m}^2$ and inertia $I = 1.59 \times 10^{-4}\,\mathrm{m}^4$. The fluid was water with density $\rho_f = 1000\,\mathrm{kg/m^3}$ and sound propagation velocity $c_f = 1500\,\mathrm{m/s}$.

In this work, we studied the 3D response of the fluid-structure system considering that the geometrical and material properties remained invariant along the z direction. The structure was modelled as a simply supported slab of thickness $t = 0.1202\,\mathrm{m}$, Young modulus $E = 2.1 \times 10^{11}\,\mathrm{N/m^2}$, Poisson's ratio $\nu = 0.3$ and density $\rho = 416\,\mathrm{kg/m^3}$. These properties gave a bending stiffness $D = Et^3/12(1-\nu^2)$ and a mass per unit length $\overline{m} = \rho t$ equivalent to the beam described in References [51, 52]. The problem discretisation was set to $1/h = 4\,\mathrm{m}^{-1}$ using a proper element order to ensure a nodal density account for the fluid wavelength $d_\lambda \geq 6$. The element order was not lower than $p = 6$ in any case according to the convergence criterion presented in Table 3.

The cut-off frequencies of the 3D coupled system for the first five propagating modes were 6.57 Hz, 20.31 Hz, 43.85 Hz, 75.95 Hz and 94.69 Hz. These results were compared to the 2D problem solution obtained by Rodríguez-Tembleque et al. [52] from a BEM-FEM model and with a FEM model when the system was subjected to a bending moment $M = M_0 e^{i\omega t}$ acting in one edge of the slab. Figure 16 shows the slab rotation at $\mathbf{x} = (10, 4, 0)$ and the natural frequencies presented by Sandberg et al. [51]. The computed response exhibited resonances at the cut-off frequencies shown in Figure 14.(c). The proposed results were in good accordance with References [51, 52].

Finally, this example examined the time domain response of the comprehensive problem produced by an impulsive bending moment. The excitation source was modelled as a Ricker pulse with a characteristic frequency $f_m = 3000\,\mathrm{Hz}$, which was defined by $B_f(\omega) = 2\omega^2/\omega_m^3 \exp(-\omega^2/\omega_m^2)$ [64], being $\omega_m = 2\pi f_m$. The 3D solution was computed as the superposition of problems with different wavenumbers in the interval

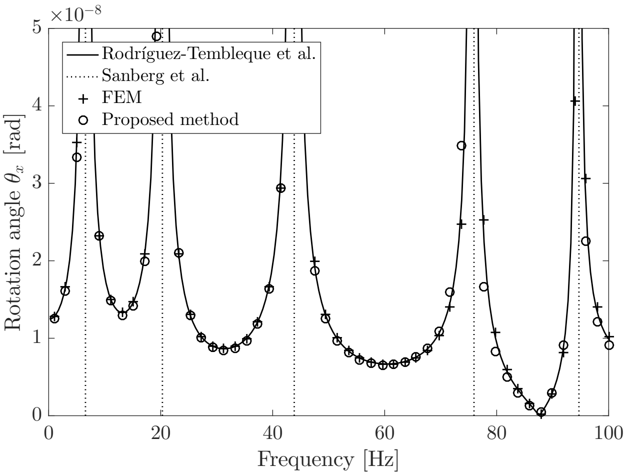

Figure 16: Rotation angle θ_x at $\mathbf{x} = (10, 4, 0)$ computed with the proposed method compared with those presented by Rodríguez-Tembleque et al. [52] and with a finite element model. The resonance frequencies presented by Sandberg et al. [51] are also indicated.

$-20.1, \mathrm{rad/m} \leq k_z \leq 20.1\,\mathrm{rad/m}$. The wavenumber sampling $\Delta k_z = 0.157\,\mathrm{rad/m}$ allowed to compute the solution for a maximum distance $z = \pi/\Delta k_z = 20\,\mathrm{m}$ from the source into a regularly spaced points with $\Delta z = 2\pi/\max(k_z) = 0.312\,\mathrm{m}$. The time domain solution was evaluated from an inverse Fourier transform of several harmonic problems in the frequency range from 10 to 10240 Hz, with a frequency sampling of $\Delta f = 10\,\mathrm{Hz}$. Complex frequencies with an imaginary part of the form $\Im(\omega) = -0.7\Delta\omega$ were used to reduce the contribution of the virtual source to the response and to prevent the occurrence of aliasing phenomenon. The effect of the imaginary part was removed in the time response applying an exponential window as $e^{0.7\Delta\omega t}$ [65].

Figure 17 shows the slab rotation and the fluid pressure at the observation point located at $\mathbf{x} = (10, 4, 0)$. The time histories showed an initial perturbation at the arrival time 0.0067 s due to waves travelling at c_f, followed by a ring of high-frequency produced by the guided wave until the time 0.0132 s. Later, a set of travelled waves struck repeatedly with higher amplitude than the first wave package.

The wave propagation was best regarded if the snapshot of the overall fluid-structure domain was studied at different times. Figures 18-21 present the slab deformation and the pressure field at four time steps. Two kinds of waves could be distinguished at $t = 0.00489\,\mathrm{s}$ (Figure 18): a low amplitude wavefront travelling at c_f followed by a slower circumferential wavefront with higher amplitude. This last mentioned wave reached the cavity bottom and was reflected toward the surface generating a high amplitude pulse at the time $t = 0.01095\,\mathrm{s}$ (Figure 19). Then, a new wavefront caused by this pulse spreading along the slab with a typical cone Mach distribution as it can be seen in Figure 20. It was repeated every time a wave travelling from the cavity bottom struck the slab (Figure 21). The wave propagation pattern became more complex as successive waves were reflected in the slab and the cavity boundaries (see the animated results in the online

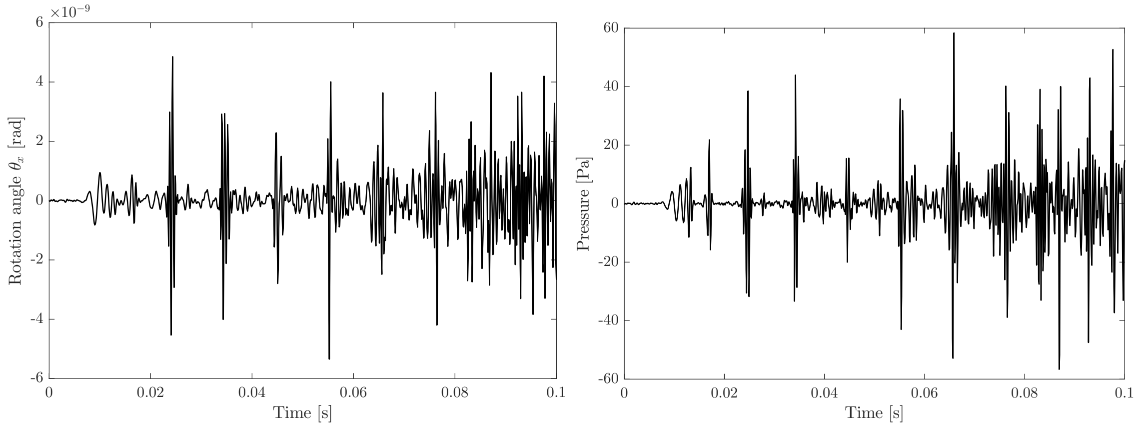

(a) (b)

Figure 17: Time response for (a) structure rotation θ_x and (b) fluid pressure at a point located at $\mathbf{x} = (10, 4, 0)$.

version). The sound wave propagation interacting with the slab structure produced an amplification of the bending waves, resulting in a repeated wave package with higher amplitude than the initial perturbation owing to the excitation.

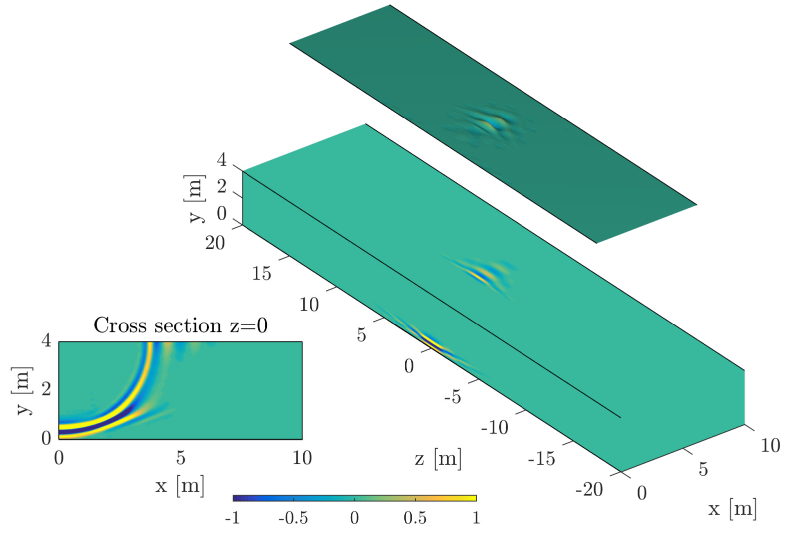

Figure 18: Fluid pressure (normalised to 4.0×10^{-5} Pa) and the vertical plate displacement (normalized to 2.3×10^{6} m) at time $t = 0.00489\,\mathrm{s}$.

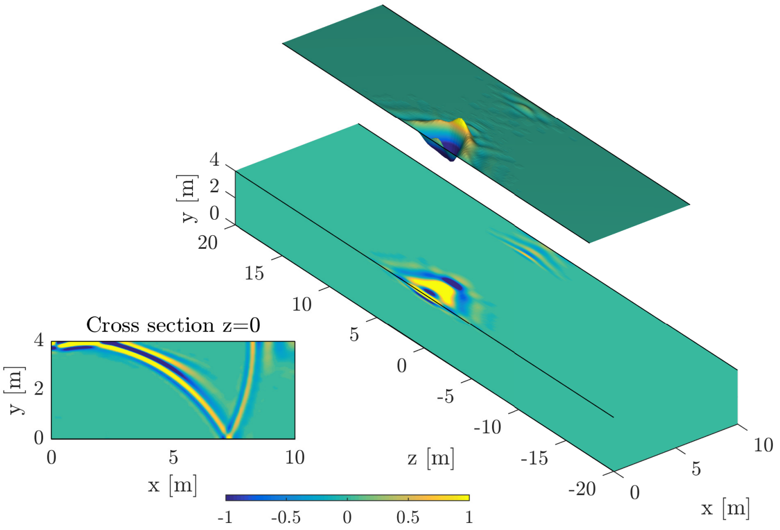

Figure 19: Fluid pressure (normalised to 4.0×10^{-5} Pa) and the vertical plate displacement (normalized to 2.3×10^{6} m) at time $t = 0.01095$ s.

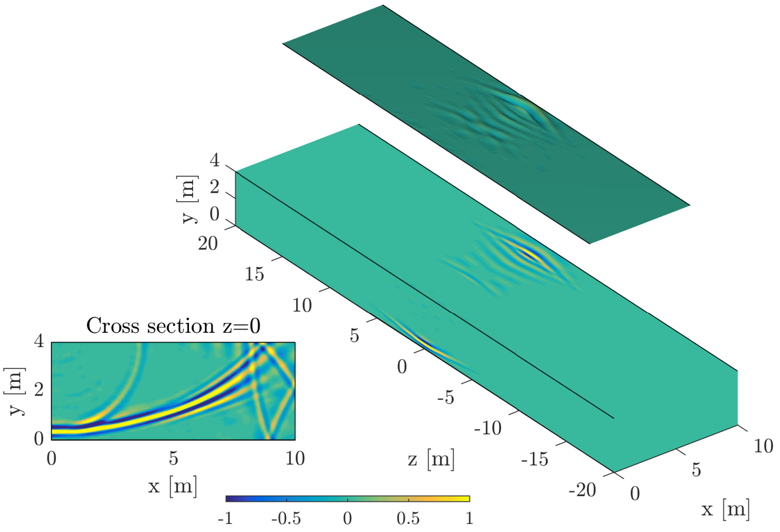

Figure 20: Fluid pressure (normalised to 4.0×10^{-5} Pa) and the vertical plate displacement (normalized to 2.3×10^{6} m) at time $t = 0.01565$ s.

4.2. Helmholtz resonator with a flexible plate

The last example studied the wave propagation in a Helmholtz resonator [53] coupled to an acoustic cavity of dimensions $W \times H = 0.01 \times 0.0025$ m (Figure 22). The cavity was subjected to an unit normal velocity $v_n = 1$ m/s acting in one edge at $z = 0$, whereas null pressure was prescribed in the opposite

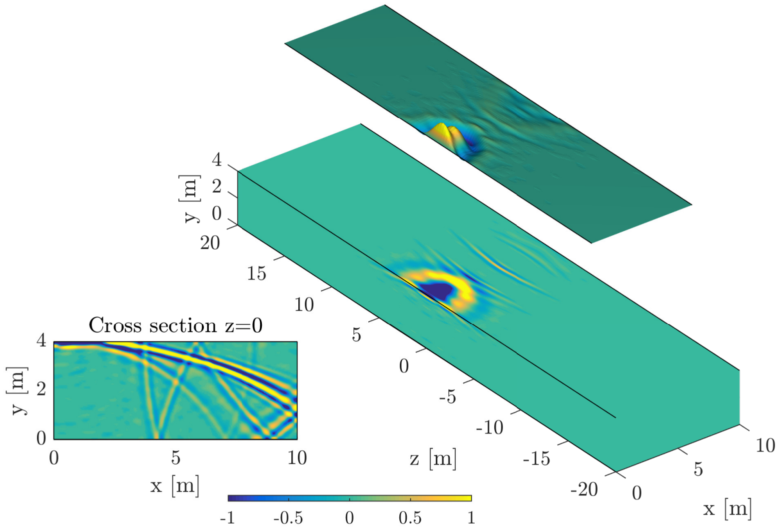

Figure 21: Fluid pressure (normalised to 4.0×10^{-5} Pa) and the vertical plate displacement (normalized to 2.3×10^{6} m) at time $t = 0.02152$ s.

side. The Helmholtz resonator had two parts: (i) a cavity with dimensions $W_c \times H_c = 0.004 \times 0.0025\,\mathrm{m}$ and (ii) a neck connector with dimensions $W_n \times H_n = 0.0013 \times 0.0012\,\mathrm{m}$. The resonator cavity had a flexible side at the bottom that was modelled as a plate (Ω_s) with thickness $t = 8.3 \times 10^{-4}\,\mathrm{m}$, Young modulus $E = 2.4 \times 10^{11}\,\mathrm{N/m^2}$, Poisson's ratio $\nu = 0.3$ and density $\rho = 7800\,\mathrm{kg/m^3}$. The plate was fixed at both ends. All the remaining boundaries were rigid with constrained velocity $v_n = 0\,\mathrm{m/s}$. The fluid had water properties with density $\rho = 1000\,\mathrm{kg/m^3}$ and sound propagation velocity $c_f = 1500\,\mathrm{m/s}$. The problem solution was computed in the frequency-wavenumber domain for 2048 frequency lines up to 1 MHz. A longitudinal wavenumber range up to $k_z = 12600\,\mathrm{rad/m}$ with a step $\Delta k_z = 200\,\mathrm{rad/m}$ was analysed. The element size was enough to ensure a minimum nodal density per wavelength $d_\lambda = 6$ by an element order $p = 6$.

The frequency response function (FRF) was computed at the midpoint of the plate for $z = 0.01\,\mathrm{m}$. This FRF (Figure 23.(a)) showed several peaks corresponding to resonance frequencies of the system. The time response was computed by the inverse Fourier transform of the FRF and it was considered an excitation source represented as a Ricker pulse with a characteristic frequency f_m. Figure 23.(b) presents the time history of the plate displacement normalised to the excitation velocity $v_n = 1\,\mathrm{m/s}$ for two different source frequencies: $f_m = 65\,\mathrm{kHz}$ and $f_m = 196\,\mathrm{kHz}$. These frequencies corresponded to the propagating mode shapes showed in Figure 24. Although the plate displacement followed an oscillating response with resonant behaviour in both cases, the maximum amplitude occurred for the second frequency since it had a higher participation factor for the plate in relation to the first mode which induced mainly an acoustic perturbation.

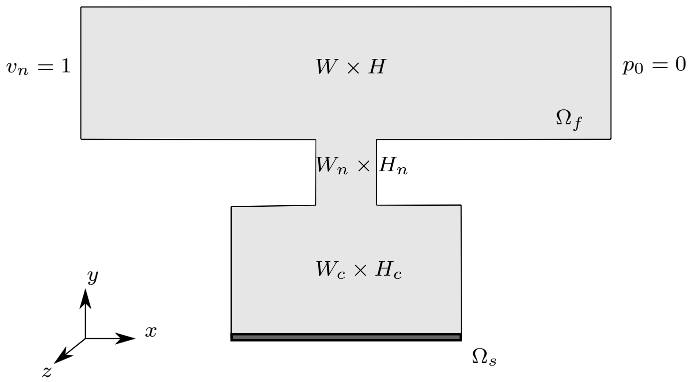

Figure 22: Helmholtz resonator with a flexible plate.

A few comments on the performance of the method in the final example with the Helmholtz resonator should be added in the end of the corresponding section.

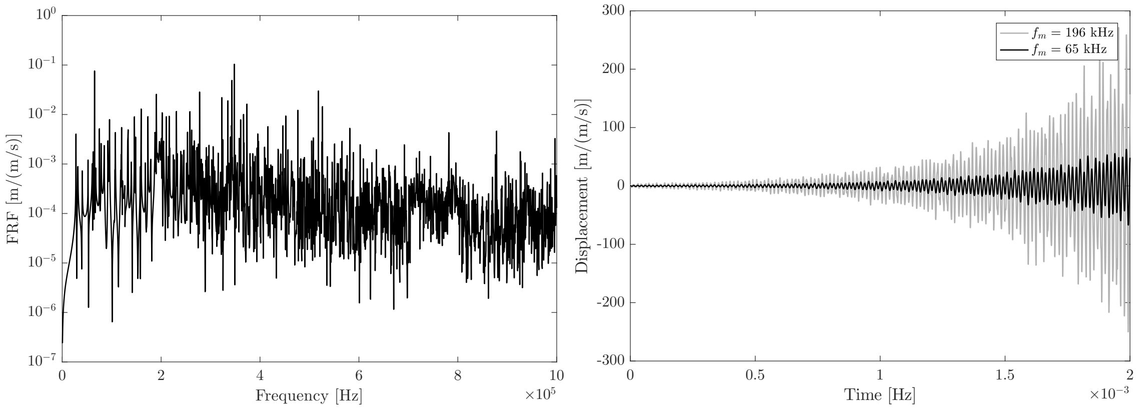

(a) (b)

Figure 23: (a) Frequency response function of plate midpoint due to a normal velocity $v_n = 1\,\mathrm{m/s}$ and (b) displacement of plate midpoint due to a Ricker pulse with a characteristic frequency f_m.

5. Conclusions

This paper has presented a new spectral element methodology to study guided waves on thin-walled structures with fluid-acoustic interaction. The method has been formulated in 2.5D and it is suitable for studying 3D problems whose material and geometric properties are homogeneous in one direction. Two novel spectral elements have been proposed to represent thin plates and acoustic cavities using Lagrange interpolation polynomials as shape functions at the Legendre-Gauss-Lobatto points.

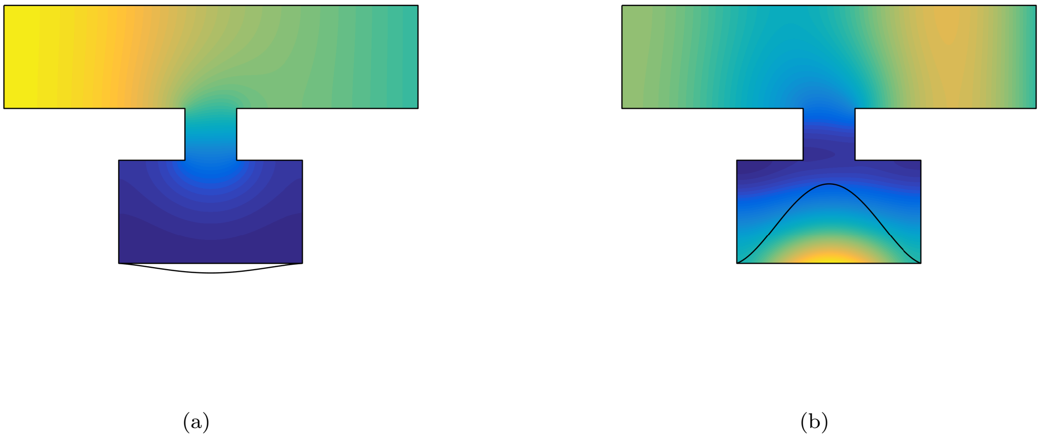
(a)

(b)

Figure 24: Fluid (colour map) and plate (solid line) propagating mode shapes at cross section $z = 0$ at frequencies: (a) 65 kHz and (b) 196 kHz.

This work has developed a C^0 plate element formulated in 2.5D based on a mixed Reissner-Mindlin/Kirchhoff-Love formulation which allows to represent thick and thin plates. The use of a substitute transverse shear strain matrix has given an element shear-locking free. The spectral fluid element in 2.5D has been derived from the Helmholtz equation. Both elements have been numerically verified from benchmark problems. The agreement with the reference solutions is quite good. The convergence analysis for different $h - p$ discretisations shows that a nodal density of six nodes per wavelength is enough to achieve the problem solution.

Finally, a time-frequency analysis was carried out in two numerical examples. In both cases, several propagating modes were identified from the frequency response function. The time response was computed by the inverse Fourier transform of the FRF for an excitation source described as a Ricker pulse. The wave propagation exhibited a complex pattern due to the FSI effects. The obtained result emphasises the importance of the fluid-structure interaction on wave guides.

Acknowledgements

The research work presented herein was supported by the Spanish Ministry of the Economy and Competitiveness (Ministerio de Economía y Competitividad) through research projects BIA2013-43085-P and BIA2016-75042-C2-1-R . This research was also supported by the project POCI-01-0247-FEDER-003344, funded by Portugal 2020 through the Operational Programme for Competitiveness Factors (COMPETE 2020). Financial support is gratefully acknowledged. The authors also wish to acknowledge the support provided by the Andalusian Scientific Computing Centre (CICA).

References

[1] V. Pagneux, N. Amir, J. Kergomard, A study of wave propagation in varying cross-section waveguides by modal decomposition. Part I. Theory and validation, Journal of the Acoustical Society of America 100 (4) (1996) 2034–22048.

[2] V. Pagneux, A. Maurel, Lamb wave propagation in elastic waveguides with variable thickness, Proceedings of the Royal Society A: Mathematical, Physical and Engineering Sciences 462 (2068) (2006) 1315–1339.

[3] J.B. Lawrie, On acoustic propagation in three-dimensional rectangular ducts with flexible walls and porous linings, Journal of the Acoustical Society of America 131 (3) (2012) 1890–1901.

[4] G.A. Athanassoulis, K.A. Belibassakis, D.A. Mitsoudis, N.A. Kampanis, V.A. Dougalis, Coupled mode and finite element approximations of underwater sound propagation problems in general stratified enviroments, Journal of Computational Acoustics 16 (1) (2008) 83–116.

[5] A. Maurel, J.-F. Mercier, V. Pagneux, Improved multimodal admittance method in varying cross section waveguides, Proceedings of the Royal Society A: Mathematical, Physical and Engineering Sciences 470 (2164).

[6] M. Bouchon, K. Aki, Discrete wave-number representation of seismic source wavefields, Bulletin of the Seismological Society of America 67 (2) (1977) 259–277.

[7] L. Gavrić, Finite Element Computation of Dispersion Properties of Thin-Walled Waveguides, Journal of Sound and Vibration 173 (1) (1994) 113–124.

[8] L. Gavrić, Computation of propagative waves in free rail using a finite element technique, Journal of Sound and Vibration 185 (3) (1995) 531–543.

[9] J.-M. Mencik, M.N Ichchou, Wave finite elements in guided elastodynamics with internal fluid, International Journal of Solids and Structures 44 (7-8) (2007) 2148–2167.

[10] C.-M. Nilsson, S. Finnveden, Waves in thin-walled fluid-filled ducts with arbitrary cross-sections, Journal of Sound and Vibration 310 (1-2) (2008) 58–76.

[11] A. Romero, A. Tadeu, P. Galvín, J. António, 2.5D coupled BEM-FEM used to model fluid and solid scattering wave, International Journal for Numerical Methods in Engineering 101 (2) (2015) 148–164.

[12] A. Romero, P. Galvín, J. António, J. Domínguez, A. Tadeu, Modelling of acoustic and elastic wave propagation from underground structures using a 2.5D BEM-FEM approach, Engineering Analysis with Boundary Elements 76 (2017) 26–39.

[13] A. Tadeu, A. Romero, P. Stanak, J. Sladek, V. Sladek, P. Galvín, J. António, Modeling elastic wave propagation in fluid-filled boreholes drilled in nonhomogeneous media: BEM-MLPG versus BEM-FEM coupling, Engineering Analysis with Boundary Elements 81 (2017) 1–11.

[14] I. Babuška, F. Ihlenburg, E.T. Paik, S.A. Sauter, A generalized finite element method for solving the Helmholtz equation in two dimensions with minimal pollution, Computer Methods in Applied Mechanics and Engineering 128 (3-4) (1995) 325–359.

[15] F. Ihlenburg, I. Babuška, S. Sauter, Reliability of finite element methods for the numerical computation of waves, Advances in Engineering Software 28 (7) (1997) 417–424.

[16] F. Ihlenburg, The medium-frequency range in computational acoustics: Practical and numerical aspects, Journal of Computational Acoustics 11 (2) (2003) 175–193.

[17] F. Ihlenburg, I. Babuška, Finite element solution of the Helmholtz equation with high wave number. Part I: The h-version of the FEM, Computers and Mathematics with Applications 30 (9) (1995) 9–37.

[18] F. Ihlenburg, I. Babuška, Finite element solution of the Helmholtz equation with high wave number. Part II: the h-p version of the FEM, SIAM Journal on Numerical Analysis 34 (1) (1997) 315–358.

[19] C. Willberg, S. Duczek, J.M. Vivar Pérez, D. Schmicker, U. Gabbert, Comparison of different higher order finite element

schemes for the simulation of Lamb waves, Computer Methods in Applied Mechanics and Engineering 241-244 (2012) 246–261.

[20] A. Deraemaeker, I. Babuška, P. Bouillard, Dispersion and pollution of the FEM solution for the Helmholtz equation in one, two and three dimensions, International Journal for Numerical Methods in Engineering 46 (4) (1999) 471–499.

[21] K.A. Belibassakis, G.A. Athanassoulis, T.K. Papathanasiou, S.P. Filopoulos, S. Markolefas, Acoustic wave propagation in inhomogeneous, layered waveguides based on modal expansions and hp-FEM, Wave Motion 51 (6) (2014) 1021–1043.

[22] A.T. Patera, A spectral element method for fluid dynamics: Laminar flow in a channel expansion, Journal of Computational Physics 54 (3) (1984) 468–488.

[23] W. Ostachowicz, P. Kudela, M. Krawczuk, A. Zak, Guided Waves in Structures for SHM: The Time-Domain Spectral Element Method, 2012.

[24] P. E.J. Vos, S. J. Sherwin, R. M. Kirby, From h to p efficiently: Implementing finite and spectral/hp element methods to achieve optimal performance for low- and high-order discretisations, Journal of Computational Physics 229 (13) (2010) 5161 – 5181.

[25] O. Z. Mehdizadeh, M. Paraschivoiu, Investigation of a two-dimensional spectral element method for Helmholtz's equation, Journal of Computational Physics 189 (1) (2003) 111 – 129.

[26] S. Petersen, D. Dreyer, O. von Estorff, Assessment of finite and spectral element shape functions for efficient iterative simulations of interior acoustics, Computer Methods in Applied Mechanics and Engineering 195 (44–47) (2006) 6463 – 6478.

[27] J. Biermann, O. von Estorff, S. Petersen, C. Wenterodt, Higher order finite and infinite elements for the solution of Helmholtz problems, Computer Methods in Applied Mechanics and Engineering 198 (13–14) (2009) 1171 – 1188.

[28] K. Christodoulou, O. Laghrouche, M.S. Mohamed, J. Trevelyan, High-order finite elements for the solution of Helmholtz problems, Computers and Structures 191 (2017) 129–139.

[29] P.E. Grafton, D.R. Strome, Analysis of axisymmetrical shells by the direct stiffness method, AIAA Journal 1 (10) (1963) 2342–2347.

[30] Y.K. Cheung, I.P. King, O.C. Zienkiewicz, Slab bridges with arbitray shape and support conditions: a general method of analysis based on finite elements, Proceedings of the Institution of Civil Engineers 40 (1) (1968) 9–36.

[31] Y.C. Loo, A.R. Cusens, The finite-strip method in bridge engineering, Spon Press, Dunfermline, United Kingdom, 1978.

[32] E. Oñate, Comparisons of finite strip method for the analysis of box grider bridges, Department of Civil Engineering. University College of Swansea, 1976.

[33] L.V. Kantorovich, V.I. Krylov, Approximate methods of higher analysis, Wiley, Groningen, Noordhoff, 1958.

[34] Y.K. Cheung, Finite Strip Method in Structural Analysis, Pergamon Press, Oxford, 1976.

[35] T.J.R. Hughes, L.P. Franca, A mixed finite element formulation for Reissner-Mindlin plate theory: Uniform convergence of all higher-order spaces, Computer Methods in Applied Mechanics and Engineering 67 (2) (1988) 223–240.

[36] K.-U. Bletzinger, M. Bischoff, E. Ramm, Unified approach for shear-locking-free triangular and rectangular shell finite elements, Computers and Structures 75 (3) (2000) 321–334.

[37] H.T.Y. Yang, S. Saigal, A. Masud, R.K. Kapania, A survey of recent shell finite elements, International Journal for Numerical Methods in Engineering 47 (1-3) (2000) 101–127.

[38] F. Gruttmann, W. Wagner, A stabilized one-point integrated quadrilateral Reissner-Mindlin plate element, International Journal for Numerical Methods in Engineering 61 (13) (2004) 2273–2295.

[39] D.J. Benson, Y. Bazilevs, M.C. Hsu, T.J.R. Hughes, Isogeometric shell analysis: The Reissner-Mindlin shell, Computer Methods in Applied Mechanics and Engineering 199 (5-8) (2010) 276–289.

[40] C. Adam, S. Bouabdallah, M. Zarroug, H. Maitournam, Improved numerical integration for locking treatment in isogeometric structural elements. Part II: Plates and shells, Computer Methods in Applied Mechanics and Engineering 284

(2015) 106–137.

[41] U. Zrahia, P. Bar-Yoseph, Plate spectral elements based upon Reissner-Mindlin theory, International Journal for Numerical Methods in Engineering 38 (8) (1995) 1341–1360.

[42] A. Chakraborty, S. Gopalakrishnan, A spectrally formulated plate element for wave propagation analysis in anisotropic material, Computer Methods in Applied Mechanics and Engineering 194 (42-44) (2005) 4425–4446.

[43] F. Birgersson, S. Finnveden, C.-M. Nilsson, A spectral super element for modelling of plate vibration. Part 1: General theory 287 (1-2) (2005) 297–314.

[44] A. Zak, A novel formulation of a spectral plate element for wave propagation in isotropic structures, Finite Elements in Analysis and Design 45 (10) (2009) 650–658.

[45] K.D. Brito, M.A. Sprague, Reissner-Mindlin Legendre spectral finite elements with mixed reduced quadrature, Finite Elements in Analysis and Design 58 (2012) 74–83.

[46] M.A. Sprague, A. Purkayastha, Legendre spectral finite elements for Reissner-Mindlin composite plates, Finite Elements in Analysis and Design 105 (2015) 33–43.

[47] J.C. Simo, D.D. Fox, M.S. Rifai, On a stress resultant geometrically exact shell model. Part III: Computational aspects of the nonlinear theory, Computer Methods in Applied Mechanics and Engineering 79 (1) (1990) 21–70.

[48] R.H. Macneal, A simple quadrilateral shell element, Computers and Structures 8 (2) (1978) 175–183.

[49] T.J.R. Hughes, T.E. Tezduyar, Finite elements based upon mindlin plate theory with particular reference to the four-node bilinear isoparametric element, Journal of Applied Mechanics, Transactions ASME 48 (3) (1981) 587–596.

[50] E.N. Dvorkin, K.-J. Bathe, A continuum mechanics based four-node shell element for general nonlinear analysis, Engineering Computations 1 (1) (1984) 77–88.

[51] G. Sandberg, P.-A. Wernberg, P. Davidson, Fundamentals of fluid-structure interaction, Computational Aspects of Structural Acoustics and Vibrations. G. Sandberg and R. Ohayon, eds Springer, Wien, 2008.

[52] L. Rodríguez-Tembleque, J.A. González, A. Cerrato, Partitioned solution strategies for coupled BEM-FEM acoustic fluid-structure interaction problems, Computers and Structures 152 (2015) 45–58.

[53] W. Akl, A. Baz, Multi-cell active acoustic metamaterial with programmable bulk modulus, Journal of Intelligent Material Systems and Structures 21 (5) (2010) 541–556.

[54] F.J. Cruz-Muñoz, A. Romero, A. Tadeu, P. Galvín, A 2.5D spectral approach to represent acoustic and elastic waveguides interaction on thin slab structures, Procedia Engineering 199 (2017), 1374–1379.

[55] O.C. Zienkiewicz, The finite element method, 3rd Edition, McGraw-Hill, 1986.

[56] L.E. Kinsler, A.R. Frey, A.B. Coppens, J.V. Sanders, Fundamentals of Acoustics, John Wiley and Sons, New York, 1982.

[57] R. Tezaur, A. Macedo, C. Farhat, R. Djellouli, Three-dimensional finite element calculations in acoustic scattering using arbitrarily shaped convex artificial boundaries, International Journal for Numerical Methods in Engineering 53 (6) (2002) 1461–1476.

[58] H. Bériot, G. Gabard, E. Perrey-Debain, Analysis of high-order finite elements for convected wave propagation, International Journal for Numerical Methods in Engineering 96 (11) (2013) 665–688.

[59] J. António, A. Tadeu, N. Simões, Response of clamped structural slabs subjected to a dynamic point load via BEM, Engineering Structures 25 (3) (2003) 293–301.

[60] K.F. Graff, Wave motion in elastic solids, Dover Publications, New York, 1975.

[61] J.M. Melenk, K. Gerdes, C. Schwab, Fully discret hp-finite elements: Fast quadrature, Computer Methods in Applied Mechanics and Engineering 190 (32-33) (2001) 4339–4364.

[62] O.C. Zienkiewicz, J.Z. Zhu, N.G. Gong, Effective and practical h-p-version adaptive analysis procedures for the finite element method, International Journal for Numerical Methods in Engineering 28 (4) (1989) 879–891.

[63] B. A. Szabó, Mesh design for the p-version of the finite element method, Computer Methods in Applied Mechanics and

Engineering 55 (1-2) (1986) 181–197.

[64] Y. Wang, Frequencies of the Ricker wavelet, Geophysics 80 (2) (2014) A31–A37.

[65] E. Kausel, J. M. Roësset, Frequency domain analysis of undamped systems, Journal of Engineering Mechanics 118 (4) (1992) 724–734.